ON EXPERIMENTAL STUDY TO EVALUATE EVAPORATION RATE OF LIQUID FUEL SPRAYS

MS. JANTARAT PROMVONGSA
ID: 52920009

A THESIS SUBMITTED AS A PART OF THE REQUIREMENTS
FOR THE DEGREE OF DOCTOR OF PHILOSOPHY
IN ENERGY TECHNOLOGY

THE JOINT GRADUATE SCHOOL OF ENERGY AND ENVIRONMENT
AT KING MONGKUT'S UNIVERSITY OF TECHNOLOGY THONBURI

2ND SEMESTER 2013

On Experimental Study to Evaluate Evaporation Rate of Liquid Fuel Sprays

Ms. Jantarat Promvongsa
ID: 52920009

A Thesis Submitted as a Part of the Requirements
for the Degree of Doctor of Philosophy
in Energy Technology

The Joint Graduate School of Energy and Environment
at King Mongkut's University of Technology Thonburi

2^{nd} Semester 2013

Thesis Committee

………………………………………………	
(Assoc. Prof. Dr. Bundit Fungtammasan)	Advisor
………………………………………………	
(Dr. Gerard Grehan)	Co-Advisor
………………………………………………..	
(Asst. Prof. Dr. Pumyos Vallikul)	Member
………………………………………………..	
(Dr. Sawitree Saengkaew)	Member
……………………………………………....	
(Prof. Dr. Ashwani Kumar Gupta)	External Examiner

Thesis Title: On Experimental Study to Evaluate Evaporation Rate of Liquid Fuel Sprays

Student's name, organization and telephone/fax numbers/email

Ms. Jantarat Promvongsa
The Joint Graduate School of Energy and Environment (JGSEE)
King Mongkut's University of Technology Thonburi (KMUTT)
126 Pracha Uthit Rd., Bangmod, Tungkru, Bangkok 10140 Thailand
Telephone: 0-8962-89973
Email: jantarat_pr@hotmail.com

Supervisor's name, organization and telephone/fax numbers/email

Assoc. Prof. Dr. Bundit Fungtammasan
The Joint Graduate School of Energy and Environment (JGSEE)
King Mongkut's University of Technology Thonburi (KMUTT)
126 Pracha Uthit Rd., Bangmod, Tungkru, Bangkok 10140 Thailand
Telephone: 0-8139-22500 or 02-470-8004
Email: bundit.fun@gmail.com

Topic: On Experimental Study to Evaluate Evaporation Rate of Liquid Fuel Sprays

Name of student: Ms. Jantarat Promvongsa **Student ID:** 52920009

Name of Supervisor: Assoc. Prof. Dr. Bundit Fungtammasan

ABSTRACT

The evaporation of a fuel spray is one of the very important processes controlling the efficiency of liquid fuel droplet combustion in engines and furnaces. A number of evaporation models of droplets in spray have been developed. However, few measurement data to quantify the evaporation of droplets in spray exists. In this thesis, experimental studies on the evaporation of an individual droplet and of line monodisperse droplets of liquid fuels have been advanced. The liquids used in this study are ethanol and distilled water.

The evaporation constant and the temperature of the droplets during evaporation are the pertinent parameters to be experimentally determined. For a single-suspended droplet of millimeter size, the imaging and the Airy –based rainbow techniques have been used to measure the time evolution of the size and the refractive index, from which the evaporation constant and the temperature of the droplets can be inferred. For the line droplets measurement, a new technique called one-dimensional rainbow technique (ORT), which is a modification of the classical global rainbow technique (GRT), is used. The ORT enables us to measure the changes of size of droplets along the line due to the evaporation at nanometric scale. The measurement data is then used to determine the evaporation constant of the droplets.

For the case of suspended water droplets, the evaporation constant and temperature obtained from the measurements are found to be dependent on the relative humidity and the temperature of the surrounding air, but independent of the size of the droplets. In this case, numerical simulation shows that the evaporation constant obtained from the measurement agrees very well with the D^2-model. The measured temperature of the droplet does not change during evaporation and being equal to the adiabatic saturation temperature of the surrounding moist air. For the ethanol, experiments under constant environmental temperature show that the regression of the D^2 with time is linear allowing one to determine the evaporation constant, being the slope of the regression line. The refractive index obtained from the rainbow measurement has the same behavior (but not the same value) as that of water, confirming that state properties of the evaporating process depend on the temperature and pressure of the ambient air.

The line droplets of ethanol are generated from an ultrasonic nozzle having initial diameter of 100-120 μm and being left to evaporate at the room temperature of 20^{o}C. The rainbow angles measured from the drops at different levels do not change, implying that all droplets along the line evaporate at a constant temperature. Over the 8 mm-line measurement length, the ethanol droplet diameter changes by 0.008 μm. With an approximated absolute drop diameter and the calculated droplet velocity, the plot of diameter squared versus time is performed, which shows the good linear regression and correlates well with the D^2-law of evaporation. The slope of the regression lines represents the evaporation constants and is found to be 0.008483±0.000513 mm^2/s.

Keywords: evaporation, d^2 law, rainbow, spray, droplet array, ethanol

ACKNOWLEDGEMENTS

First and foremost, I would like to take this time to thank the Thai Research Fund (TRF) for all their financial support to me through the Golden Jubilee Ph.D. Program in order to make this thesis possible.

Thanks to my advisors, Assoc. Prof. Dr. Bundit Funtammasan and Asst. Prof. Dr. Pumyos Vallikul, for offering me an opportunity to study and get a grateful experience, for the continuous support of my Ph.D. study and research, and for their patience and kindness.

I am grateful to my advisor from France, Dr. Grehan Gerard, and to Dr. Sawitree Saengkaew for expanding my knowledge in the optical techniques, especially in the beautiful and wonderful Rainbow technique. Appreciate for a warm welcome when I went to France, for your helpfulness and kindness. I have learned a lot from you about the optical techniques and doing a research.

Besides my advisors, I would like to thank the external research examiner, Prof. Dr. Ashwani K. Gupta, for his encouragement, insightful comments, and remarkable questions.

My sincere thanks also go to all my friends in Fluid-Optics Interaction Research laboratory (FOIRe) at King Mongkut's University of Technology North Bangkok and my friends at CORIA-CNRS for the good friendship, for sharing their knowledge and experimental instruments. Thanks to JGSEE officers for advising me how to work on formal documents.

Last but not the least, I would like to thank my family and my friends who are always beside me and support me throughout my life.

CONTENTS

CONTENTS (Cont')

LIST OF TABLES

LIST OF FIGURES

LIST OF FIGURES (Cont')

LIST OF FIGURES (Cont')

LIST OF SYMBOLS

A	Surface area (m^2)
B_M	Mass transfer number (-)
B_T	Heat transfer number (-)
c_p	Constant pressure specific heat (J/kg K)
D	Drop diameter (m)
D_{AB}	Binary diffusivity (m^2/s)
k	Thermal conductivity (W/m K)
L	Heat of vaporization (J/kg)
$\dot{m}$	Mass flow rate (kg/s)
N	Molar number (mol)
Nu	Nusselt number (-)
P	Pressure (Pa)
Pr	Prandtl number (-)
P_{ref}	Reference pressure (Pa)
R	Universal gas constant (= 8.3145 J/mol K)
r	Radial direction, droplet radius (m)
RH	Relative humidity (%)
Sc	Schmidt number (-)
Sh	Sherwood number (-)
T	Temperature (^{o}C)
t	Time (s)
T_{ab}	Adiabatic saturation temperature (^{o}C)
T_{db}	Dry bulb temperature (^{o}C)

T_{ref}	Reference temperature (^{o}C)
v	Bulk velocity (m/s)
W	Molacular weight (kg/mol)
X_{mgs}	Mole fraction on the gas side (-)
X_{mls}	Mole fraction on the liquid side (-)
Y	Mass fraction (-)
α	Thermal diffusivity (m^2/s)
β	Evaporation constant (m^2/s)
ε_m	Fractional vaporization rate (-)
ρ	Density (kg/m^3)
ω	Humidity ratio (kg water/kg air)

subscripts

a	Dry air
F	Fuel or evaporating liquid
l	Liquid phase
s	Droplet surface
w	Water
∞	Surrounding gas

CHAPTER 1
INTRODUCTION

1.1 Rationale/ Problem Statement

The continued use of fossil fuel results in the depletion of fossil fuel resources, and at the same time, increases substantially the amount of greenhouse gas emissions. A number of renewable energy resources have been introduced to reduce fossil fuel consumption. Technologies to convert such sources, such as solar energy, wind and hydropower, into energy have been successfully developed and deployed in many countries. In recent years, technologies for the production and utilization of biofuel – a renewable fuel that is gaining increasing significance, have also been developed or improved, particularly the use of ethanol in the spark ignition engines and biodiesel in the compression ignition engines. However these biofuels possess properties that different to conventional liquid petroleum fuel and their evaporation and combustion behaviors are not yet well understood.

Biofuels are fuels that are made from living organisms (usually plants). The biofuels mostly used in transportation are ethanol and biodiesel. Ethanol is usually blended with gasoline while biodiesel is blended with regular diesel to substitute a portion of petroleum fuel and to reduce greenhouse gas emissions. The properties of biofuels are different from those of petroleum fuels and depend also on the type of biofuel resource. Using biofuels with existing technologies, which are originally designed for petroleum fuels, may thus lead to inefficient energy conversion. Therefore characterization of the physical-chemical properties affecting combustion processes is important for determining the optimum operating conditions for such energy conversion technologies.

Among the fuel properties, the evaporation rate of liquid fuel spray is one of the most important parameters determining the effectiveness of energy conversion processes of heat producing devices using spray technology. The study of Warnatz J. et,al. [1] shows that 50% of the cycle time of the combustion in diesel engines is consumed by the evaporation process. Then, the evaporation rate becomes the parameter controlling the combustion time of the engine. However, despite continued study on the subject, both measurement and prediction techniques to determine the evaporation rate remain current research challenges. These are due to the hostile environment of the spray that limits the application of classical intrusive probe measurement techniques.

This thesis proposes alternative means to evaluate the evaporation rate of the spray droplets under room temperature environments. The evaporation constant will be directly measured on a single droplet via the direct image analyses technique. The temperature of droplet is investigated instantaneously by using the rainbow technique. A modified global rainbow technique named one dimension rainbow technique (ORT) is used to measure the evaporation rate of droplets in spray.

1.2 Objectives

The main objectives of this thesis are to develop an advanced experimental technique for accurately determining the size and temperature of evaporating liquid – fuel drops in a spray, and to develop a mathematical model for evaluating their evaporation rate from the measured data. Specifically the measurement technique and model developed are aimed at investigating the evaporation of biofuels that are widely used in Thailand. Ultimately, this research will provide useful data for the combustion studies in engines and furnaces using biofuels and background information for the specification of biofuel standards in Thailand.

1.3 Literature Review

Studies on the evaporation of a single liquid drop can be found in many research works [2-5]. Theoretically, the evaporation model for a single drop is based on heat and mass conservation of the drop in gas phase [6]. This in turn constitutes a boundary value problem of partial differential equations governing the transfer processes of gaseous mixture surrounding the drop, with the gas phase properties at the drop’s surface and at the infinite distance from the drop’s surface being the boundary conditions to the problem. When diffusion heat transfer is considered, as the only mode of heat feeding thermal energy to the evaporating drop at an elevated ambient temperature, the evaporation follows the D^2 –law, which states that the square of the drop diameter decreases linearly with time. In classical studies, the evaporation time of a single drop is measured through a series of images taken during evaporation against the evolution time.

Marshall [7, 8] and Lefbvre [9] investigated the evaporation of individual drops of diameter around 0.7-1 mm, suspending from a wire. Experimental studies showed that the diameter of the drop obtained from its time dependent 2-D images decreases in accordance with the D^2 –law. The evaporation constant, which is the slope of the D^2 versus time, increases when temperature increases. The influence of pressure on the evaporation constant is however dependent on the ambient temperature. If the ambient temperature is set to be lower than the boiling point of the liquid then the evaporation constant decreases with increasing pressure and vice versa [9]. In a more complex situation, when the convective heat transfer mode at a finite Reynolds number is taken into account, the evaporation no longer follows the D^2 –law. In this case the diameter of order 3/2 for laminar flow and of order one for turbulent flow [10] varies with time.

Morin et,al. [2] used the suspended drop technique to determine the evaporation constant of biofuels. The liquid fuels were methyl ester of rape seed oil and of sun flower oil methyl. The ambient temperatures were set at higher range between 473 and 1020 K. A distinct phenomenon for heating of these biofuels, as compared to conventional fuels or water drops, is that dilatation presents at the beginning of the evaporation of biofuels. In their work, the evaporation process of biofuels are divided into 2 stages: the first stage is unsteady phenomena beginning at the initial heating, dilation, evaporation of the drop and ending when the drop diameter decreases to its initial diameter. The second stage is steady state evaporation; during which the linear fit for the evaporation constant can be done from the experimental data.

Using the suspended drop technique in an experimental study to observe the evaporation process of spherical drops has a drawback in that the shape of the droplet and that the wire modified the heat exchange, including fluid circulation inside the droplet. To relax these constraints, non-suspended drop experiments have been performed. Moyle et al [11] generated microscale water drops ranging from 15 to 50 microns injected into a particle trap using AC field of a cubic electrodynamics levitation cell [12]. The ambient to the water drops is horizontal laminar flow of N_2 containing a known concentration of water vapor. A snapshot of the images of Mie interference patterns of the drops is indirectly used to view the sizes of the particles at the evolution time. Mass accommodation coefficient of the particular flow has been obtained from the best fit of the evaporative cooling mass transfer model to the experimental data. The model fitted the experimental data very well.

There is also the situation of the flow over the drop at low Reynolds number with combustion flames either surrounding the drops or at the wake behind the drops. It has been shown numerically that the flame configuration depends on the value of Damkolher number (the ratio of chemical to advection effects). At lower Damkolher number, the combustion flame appears at the wake region behind the drop whereas at higher Damkoler number the flame envelop confines the drop, speeding up the burn-out time [13].

The measurement on evaporation of spray needs more delicate procedures than those for a single drop because the drops are quite small (10-100 μm), and there is randomness in the drop position and size. Optical techniques have been widely used in spray characterization because they are non-intrusive and sensitive to small length scale objects. For biodiesel spray generated from a small industrial burner, drop size distributions of the droplets spatially distributed along the line of sight measurement have been measured using Malvern instrument [14]. Tantivoranukul et al applied D^2 –law to each class of drop-size distribution of the spray to predict the time evolution of the distributions and evaporation time of the biodiesel spray. In their work, the drop interactions effects on the evaporation were omitted.

Rainbow refractometry is one alternative technique to measure liquid drop diameter and temperature. More recently, inversion of global-rainbow signals obtained from sprays have been used to determine a drop's mean temperature and the drop-size distribution. It has been found that the refractive index errors by 0.001 when ellipticity is between 0.999 and 1.001 [15]. This makes the technique a very attractive mean to determine liquid drops temperature at the earlier atomization stages (primary/secondary). The measurements of size distribution and refractive index of a pure biodiesel spray by using global rainbow technique based on Nussenzvieg theory are successfully achieved for the first time [16].

CHAPTER 2

THEORIES

2.1 Evaporation Models

Many evaporation models of fuel droplets have been studied. From the classification of Sirignano [17], evaporation models can be divided into 6 groups in ascending order of complexity as follows:

(1) models of the uniform droplet temperature and constant with time;
(2) models of the infinite thermal conductivity of liquid (no temperature gradient inside the droplet);
(3) models of the finite thermal conductivity of liquid but no re-circulation inside the droplet (conduction limit);
(4) models that take into account both finite thermal conductivity of liquid and the re-circulation in terms of the correction factor (effective conductivity models)
(5) models describing the re-circulation inside the droplet in terms of vortex dynamics (vortex model)
(6) models based on the full solution of the Navier-Stokes Equation.

The first group is the most attractive for the analytical studies of evaporation. It is adequate to approximate the evaporation of the stagnant droplet without combustion. Thus, this work will focus on this model. In particular, the states at the droplet surface, such as temperature and species concentration, are assumed to be saturation vapor. The state at the drop surface can be explained and approximated by the concept of the adiabatic saturation process, which is detailed in Section 2.1.1. Section 2.1.2 presents the evaporation model of the exact solution of the heat and mass transfer equation. From this model, the mass flux or the evaporation constant of droplet can be calculated. However, the finite different method, as presented in Section 2.1.3, is still attractive. It gives the temperature and concentration profiles that enable us to have a better understanding of the evaporation behavior.

2.1.1 Adiabatic Saturation Process

The concept of the adiabatic saturation process can be found in many engineering textbooks [18, 19]. This concept can be used to explain the temperature partial pressure and mass fraction at the surface of the evaporating liquid in any shape.

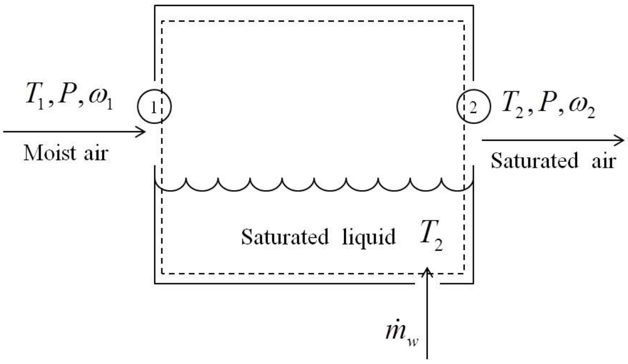

Figure 2.1: A system of liquid evaporation in the adiabatic saturation process

Consider a control volume containing a liquid bath, with a moist air inlet and an outlet across the system boundary, as shown in Fig. 2.1. The moist air enters the control surface at the temperature equal to the dry bulb temperature,T_1, and having humidity ratio, ω_1. The liquid in the liquid bath is assumed to be the saturated liquid at the saturated temperature, T_2. The moist air in the control volume feeds energy to the liquid just enough to vaporize the liquid on its surface; and the evaporation rate of liquid is equal to the supplied mass flow rate, $\dot{m}_F$. The liquid evaporates to the air until the air becomes the saturated air at the exit of the control volume. The energy balance can be written as

$$c_{pa}T_1 + \omega_1 h_{g@T_1} + \omega_2 h_{f@T_2} = \omega_2 h_{g@T_2} . \tag{2.1}$$

Then,

$$c_{pa}(T_1 - T_2) + \omega_1 h_{g@T_1} = (\omega_2 - \omega_1) h_{fg@T_2} , \tag{2.2}$$

where

$$\omega_2 = \frac{m_F}{m_a} = \frac{P_F / R_F}{P_a / R_a} = \frac{P_F / R_F}{(P - P_F) / R_a} . \tag{2.3}$$

The value of ω_1 is the humidity ratio of the surrounding air in the case of the water droplet. For a liquid fuel, ω_1 is assumed to be zero. The partial pressure of fuel is the saturated pressure corresponding to the surface temperature which can be calculated by Clausius-Claperon equation as

$$P_F = P_{ref} \exp\left(\frac{L_F (T_s - T_{ref})}{RT_s T_{ref}} \right), \tag{2.4}$$

where P_{ref} and T_{ref} are the reference pressure and temperature of fuel. $R = 8.3145$ J/mol·K is the universal gas constant. Another equation that approximates the vapor pressure of the liquid is the Antoine Equation. It is written as

$$P_F = \exp\left(A - \left(\frac{B}{T + C} \right) \right); \tag{2.5}$$

where A, B and C are the constant values for the substance. The mass fraction of fuel vapor at the drop surface is

$$Y_{Fs} = \frac{\omega_F}{1 + \omega_F}. \tag{2.6}$$

Since most properties of the fuel vapor are temperature-dependent, the iteration process is used to determine the surface temperature.

2.1.2 Exact Solution

The solutions to the heat and mass transfer equations have been determined to provide the simple model for evaporation prediction. However, the model does not cover all situations of evaporation depending on the assumptions that it was based on. This study focuses on the evaporation of the spherical droplet without combustion based on the assumption that there is no temperature gradient inside the droplet (infinite thermal conductivity of liquid). The evaporation of the stagnant droplet (non-convective flow) and of the moving droplet is reviewed in this section.

The diffusion heat and mass transfer model governing the diffusion processes of a quasi-steady ideal gas phase evaporated from a perfectly spherical drop was advanced in 1953 by Spalding [6]. The heat and mass fuel vapor diffuse through the drop surface when the necessary amount of heat has been supplied from the ambient to the vaporizing liquid drop. The equations governing the one-dimensional diffusions of energy and of the fuel vapor are

$$r^2 \rho v \frac{dc_p T}{dr} = \frac{d}{dr}\left(\frac{r^2 k}{c_p}\frac{dc_p T}{dr}\right) \tag{2.7}$$

$$r^2 \rho v \frac{dY_F}{dr} = \frac{d}{dr}\left(r^2 \rho D_{AB}\frac{dY_F}{dr}\right) \tag{2.8}$$

where T and Y_F is, respectively, the temperature and mass fraction of fuel at any radius r, ρ, c_p, D_{AB} and k are respectively, density, specific heat, mass diffusion coefficient and conductivity coefficient of the fuel vapor. With this equation, the fuel vapor from the droplet surface to the outer region is considered. Boundary conditions are imposed at the surface and at the infinite distance from the center of the drop. At the surface, heat conducting through the drop is balanced with the heat carrying out from the surface by evaporation, hence

$$-k\left(\frac{dT}{dr}\right)_s = \rho_s v_s L \tag{2.9}$$

where v and L are the bulk velocity and latent heat, respectively. The subscript s represents the fuel vapor-gas mixture condition at the drop surface. Also the mass flux leaving the surface is equal to the sum of the fuel mass flow rate due to convection and diffusion.

$$\rho_s v_s = \rho_s v_s Y_F - \rho_s D_{AB}\left(\frac{dY_F}{dr}\right)_s \tag{2.10}$$

At the infinite distance from the drop, the gaseous temperature and the mass fraction of the fuel are those at the ambient conditions: T_∞ and $Y_{F\infty}$ respectively. The analytical solutions to the transport equations give

$$r_s v_s = \alpha_s \ln(1+B_T) = D_{AB} \ln(1+B_M), \tag{2.11}$$

where $\alpha_s = \frac{k}{\rho c_p}$ is the thermal diffusivity. Subscript l indicates the properties of the liquid inside droplet. B_M and B_T are mass and heat transfer numbers, which are, respectively:

$$B_T = \frac{c_{pg}\left(T_\infty - T_s\right)}{L}, \tag{2.12a}$$

and

$$B_M = \frac{Y_{Fs} - Y_{F\infty}}{1 - Y_{Fs}}. \tag{2.12b}$$

where c_{pg} the heat capacity and the latent heat of the fuel vapor-gas mixture at the drop surface. The rate of mass flux transfer through the drop surface can be written as:

$$\dot{m}'' = \rho_s v_s = \frac{\rho_s D_{AB}}{r_s} \ln(1 + B_M) = \frac{\rho_s \alpha_s}{r_s} \ln(1 + B_T). \tag{2.13}$$

The analytical solution is obtained from the assumption of the constant diameter. To connect the solution to the time variation drop diameter, the mass continuity equation is considered to be:

$$\dot{m} = \rho_s v_s A_s \tag{2.14}$$

$$\rho_l \frac{d(\pi D^3 / 6)}{dt} = \rho_s v_s \pi D^2 \tag{2.15}$$

The integration of Eq. 2.13 yields

$$D^2 = D_o^2 - \beta t, \tag{2.16}$$

where D and D_o are drop diameter at any time t and at time $t=0$ respectively, and:

$$\beta = \frac{8\rho_s D_{AB}}{\rho_l} \ln(1 + B_M) = \frac{8\rho_s \alpha_s}{\rho_l} \ln(1 + B_T). \tag{2.17}$$

This is the classical theory of evaporation that is normally used to describe the evaporation behavior of a spherical droplet in the quasi-steady state, namely the D^2-law. In many evaporation studies, the evaporation constant, β, is referred as the evaporation characteristic of the fuel. The experimental study on the evaporation of liquid drop based on the D^2-law has been done in many works [10, 20, 21]. However, this solution does not take into account the effect of the convective flow. Therefore, the evaporation model described so far will lead to underestimation if the moving droplet is considered. To take into account convection, heat transfer coefficient, h, and mass transfer coefficient, h_m, are normally represented in the terms of Nusselt number, Nu, and Sherwood number, Sh, which are:

$$Nu = \frac{hD}{k} \tag{2.18a}$$

and
$$Sh = \frac{h_m D}{D_{AB}}. \tag{2.18b}$$

The fractions of Nu and Sh referred to those values of the non-evaporating droplet, Nu_0 and Sh_0, introduced as:

$$Nu = \frac{\ln(1+B_T)}{B_T} Nu_0, \tag{2.19a}$$

$$Sh = \frac{\ln(1+B_M)}{B_M} Sh_0. \tag{2.19b}$$

Nu_0 and Sh_0 for the moving droplets can be determined by:

$$Nu_0 = 2 + \beta_c \mathrm{Re}^{1/3} \mathrm{Pr}^{1/3}, \tag{2.20a}$$

$$Sh_0 = 2 + \beta_c \mathrm{Re}^{1/3} Sc^{1/3}. \tag{2.20b}$$

where the value of coefficient β_c can be determined either from experiment or complex numerical analysis. The widely used values of this coefficient are 0.6 [22], 0.57 [23] and 0.552 [24]. Note that in the case of the stagnant and non-evaporating droplet, Re→0, $Nu_0 = Sh_0 = 2$. Substituting Eq. 2.19 into Eq. 2.13 obtains:

$$\dot{m}'' = \frac{\rho_s D_{AB}}{2r_s} Sh B_M = \frac{\rho_s \alpha_s}{2r_s} Nu B_T. \tag{2.21}$$

The film theory was developed by Abramzon and Sirignano [17] to improve the accuracy for the evaporation rate approximation. They defined the modified Nusselt number and Sherwood number in the form:

$$Nu^* = 2 + \frac{Nu_0 - 2}{F_T}, \tag{2.22a}$$

$$Sh^* = 2 + \frac{Sh_0 - 2}{F_M}, \tag{2.22b}$$

where

$$F_{M(T)} = (1 + B_{M(T)})^{0.7} \frac{\ln(1 + B_{M(T)})}{B_{M(T)}}. \tag{2.23}$$

Then, the values of Nu and Sh are calculated from Eq. 2.7 by replacing Nu_0 and Sh_0 by Nu^* and Sh^*, which:

$$Nu = \frac{\ln(1 + B_T)}{B_T}\left(2 + \frac{Nu_0 - 2}{F_T}\right), \tag{2.24a}$$

$$Sh = \frac{\ln(1 + B_M)}{B_M}\left(2 + \frac{Sh_0 - 2}{F_M}\right). \tag{2.24b}$$

The evaporation model described previously is based on the assumption of the pure substance liquid. The multi-component droplet models have been summarized by Marshall [17], and will be reviewed. In the multi-component case, the fractional vaporization rate, ε_m, is used to define the mass flux fraction and the species evaporation rate for species m as:

$$\rho v \varepsilon_m = \rho v Y_m - \rho D \frac{\partial Y_m}{\partial n}, \tag{2.25}$$

and

$$\dot{m}_m = \varepsilon_m \dot{m} \tag{2.26}$$

The latent heat of the fuel becomes

$$L = \sum_m \varepsilon_m L_m \tag{2.27}$$

Nu, Sh and B_T can be calculated using the equation of the pure substance droplet, Eq. 2.19 or Eq. 2.22 and Eq. 2.12a. Assuming that the diffusion coefficients are equal for all components the mass transfer numbers for all species are then identical, which can be written as:

$$B_M = B_m = \frac{Y_{m,s} - Y_{m,\infty}}{\varepsilon_m - Y_{m,s}} \tag{2.28}$$

Mass fraction of the species m at the droplet surface can be determined from the Clausius-Clapeyron equation of the ratio of the mole fraction on the gas side of drop surface, X_{mgs}, to that on the liquid side, X_{mls}, that is:

$$\frac{X_{mgs}}{X_{mls}} = \frac{1}{p}\exp\left[\frac{L_m}{R_m}\left(\frac{1}{T_{b,m}} - \frac{1}{T_s}\right)\right]. \tag{2.29}$$

Then, the mass fraction, Y_m, is calculated by:

$$Y_m = \frac{X_m W_m}{\sum_i X_i W_i}, \tag{2.30}$$

where W_m is the molecular weight of species *m*.

2.1.3 Numerical Solution

For a better understanding of the heat and mass transfer behavior in the evaporation process, the profiles of temperature and mass fraction from the drop surface to its surrounding are determined. To obtain the solutions, Eq. 2.7 is solved alongside with Eq. 2.8 by using a numerical method. Considering the heat transfer problem, a liquid drop is evaporated within a controlled environmental temperature, T_∞. The heat flux to the surface, $k\frac{dT}{dr}$, is equal to the rate of evaporative cooling heat flux carried out of the particle surface, $\rho_s v_s \Delta h_v$. The solution to the equation is the temperature distribution within the gas phase when the temperature, T_s, of the drop is given. The continuum between drop surface (r_s) to the specified distance far away from droplet (r_∞) was discretized into N grids as demonstrated in Fig. 2.2.

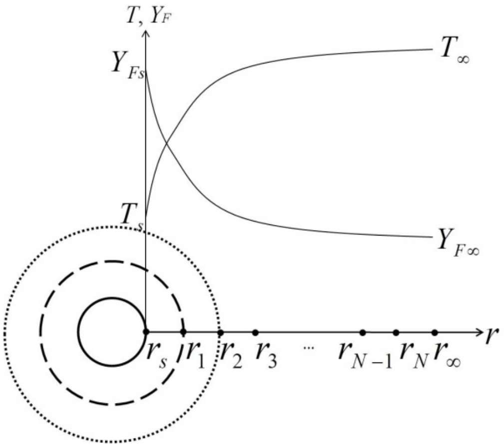

Figure 2.2: The schematic diagram of the discrete point within the continuum

Energy Equation:

$$r_s^2 \rho_s v_s \frac{dT}{dr} = \frac{d}{dr}\left(r^2 \frac{k}{c_p} \frac{dT}{dr} \right)$$

BCs:

$$r = r_s : k\frac{dT}{dr} = \rho_s v_s L \text{ and } r = r_\infty : T = T_\infty$$

That is discrete to

$$\frac{k}{2\Delta r}\left(-3T_s + 4T_1 - T_2\right) = \rho_s v_s L$$

Then, value of v_s can be determined from the temperature profile:

$$v_s = \left(-3T_s + 4T_1 - T_2\right)\frac{k_s / 2\Delta r}{\rho_s L}$$

For a unitary of the Lewis number:

$$\rho D = \rho_s D_{AB} = \frac{k}{c_p}$$

Discrete the energy equation and determine T_s that satisfies the gas phase equation, then for $i = 1$

$$\left(\frac{4r_s^2 + 4r_2^2}{2\Delta r / \rho_s D_{AB}}\right)T_1 + \left(r_s^2 \rho_s v_s - \frac{r_s^2 + 3r_2^2}{2\Delta r / \rho_s D_{AB}}\right)T_2 = \left(r_s^2 \rho_s v_s + \frac{3r_s^2 + r_2^2}{2\Delta r / \rho_s D_{AB}}\right)T_s$$

For i=2:N-1

$$\left(-r_s^2\rho_s v_s - \frac{r_{i+1}^2 + 3r_{i-1}^2}{2\Delta r/\rho_s D_{AB}}\right)T_{i-1} + \left(\frac{4r_{i+1}^2 + 4r_{i-1}^2}{2\Delta r/\rho_s D_{AB}}\right)T_i + \left(r_s^2\rho_s v_s - \frac{3r_{i+1}^2 + r_{i-1}^2}{2\Delta r/\rho_s D_{AB}}\right)T_{i+1} = 0$$

and at i=N

$$\left(-r_s^2\rho_s v_s - \frac{r_\infty^2 + 3r_{N-1}^2}{2\Delta r/\rho_s D_{AB}}\right)T_{N-1} + \left(\frac{4r_{N-1}^2 + 4r_\infty^2}{2\Delta r/\rho_s D_{AB}}\right)T_N = \left(-r_s^2\rho_s v_s + \frac{3r_\infty^2 + r_{N-1}^2}{2\Delta r/\rho_s D_{AB}}\right)T_\infty .$$

Consider the mass transfer problem, a liquid drop is evaporating within a controlled environmental temperature, T_∞. The mass fraction, $Y_A(r)$, and mass flux, ρv_r, along radius, r, from the surface of the drop are to be determined when the temperature, T_s, of the drop is given. The continuum between drop surface (r_s) to the specified distance far away from droplet (r_∞) was discretized into N grids as demonstrated in Fig. 2.2.

From the continuity equation,

$$\frac{d}{dr}\left(r^2\rho v_r\right)$$

we obtain

$$r^2\rho v_r = r_s^2\rho_s v_s\text{=constant.}$$

The first discrete point i = 1, using 1st order backward difference:

$$\rho_1 v_1 = \frac{r_s^2\rho_s v_s}{r_1^2}$$

The interior points i = 2 to N use 2nd order backward difference:

$$\rho_i v_i = \frac{4r_{i-1}^2\rho_{i-1}v_{i-1} - r_{i-2}^2\rho_{i-2}v_{i-2}}{6\Delta r r_i^2}$$

Species equation:

$$r^2\rho v\frac{dY_F}{dr} = \frac{d}{dr}\left(r^2\rho D_{AB}\frac{dY_F}{dr}\right)$$

Phase equilibrium gives the surface condition as

$$\rho_s v_s = \rho_s v_s Y_F - \rho_s D_{AB}\left(\frac{dY_F}{dr}\right)_s$$

The first discrete point i = 1, using 2nd order central difference:

$$\frac{-r_s^2\rho_s v_s Y_s + r_2^2\rho_2 v_2 2Y_2}{2\Delta r} = \frac{-r_s^2\rho_s D_{AB}(dY_A/dr)_s + r_2^2\rho_2 D_{AB}\left(dY_A/dr\right)_2}{2\Delta r}.$$

At r = r$_s$ using 2nd order forward difference and at i = 2 use 2nd order backward difference for the derivative terms.

$$-r_s^2\rho_s v_s Y_s + r_2^2\rho_2 v_2 2Y_2 = \frac{-r_s^2(-3Y_s+4Y_1-Y_2)+r_2^2(Y_s-4Y_1+3Y_2)}{2\Delta r/\rho_s D_{AB}}$$

$$-r_s^2\rho_s v_s Y_s + r_2^2\rho_2 v_2 2Y_2 = \frac{3Y_s r_s^2+Y_s r_s^2}{2\Delta r/\rho_s D_{AB}} + \frac{-4Y_1 r_s^2+Y_2 r_s^2-4Y_1 r_2^2+3Y_2 r_2^2}{2\Delta r/\rho_s D_{AB}}$$

$$-r_s^2\rho_s v_s Y_s - \left(\frac{3Y_s r_s^2+Y_s r_s^2}{2\Delta r/\rho_s D_{AB}}\right) + \left(\frac{-4Y_1 r_s^2-4Y_1 r_2^2}{2\Delta r/\rho_s D_{AB}}\right) + r_2^2\rho_2 v_2 Y_2 - \left(\frac{Y_2 r_s^2+3Y_2 r_2^2}{2\Delta r/\rho_s D_{AB}}\right) = 0$$

Therefore at $i = 1$

$$\left(\frac{4r_s^2+4r_2^2}{2\Delta r/\rho_s D_{AB}}\right)Y_1 + \left(r_s^2\rho_s v_s - \frac{r_s^2+3r_2^2}{2\Delta r/\rho_s D_{AB}}\right)Y_2 = \left(r_s^2\rho_s v_s + \frac{3r_s^2+r_s^2}{2\Delta r/\rho_s D_{AB}}\right)Y_s$$

For $i = 2{:}N-1$

$$\left(-r_s^2\rho_s v_s - \frac{r_{i+1}^2+3r_{i-1}^2}{2\Delta r/\rho_s D_{AB}}\right)Y_{i-1} + \left(\frac{4r_{i+1}^2+4r_{i-1}^2}{2\Delta r/\rho_s D_{AB}}\right)Y_i + \left(r_s^2\rho_s v_s - \frac{3r_{i+1}^2+r_{i-1}^2}{2\Delta r/\rho_s D_{AB}}\right)Y_{i+1} = 0$$

At $i = N$

$$\left(-r_s^2\rho_s v_s - \frac{r_\infty^2+3r_{N-1}^2}{2\Delta r/\rho_s D_{AB}}\right)Y_{N-1} + \left(\frac{4r_{N-1}^2+4r_\infty^2}{2\Delta r/\rho_s D_{AB}}\right)Y_N = \left(-r_s^2\rho_s v_s + \frac{3r_\infty^2+r_{N-1}^2}{2\Delta r/\rho_s D_{AB}}\right)Y_\infty$$

Determine v_s from the mass fraction profile:

$$v_{s,new} = \frac{D_s(-3Y_s+4Y_1-Y_2)}{2\Delta r(Y_s-1)}$$

The simulation method can be done following the flow chart on the next page.

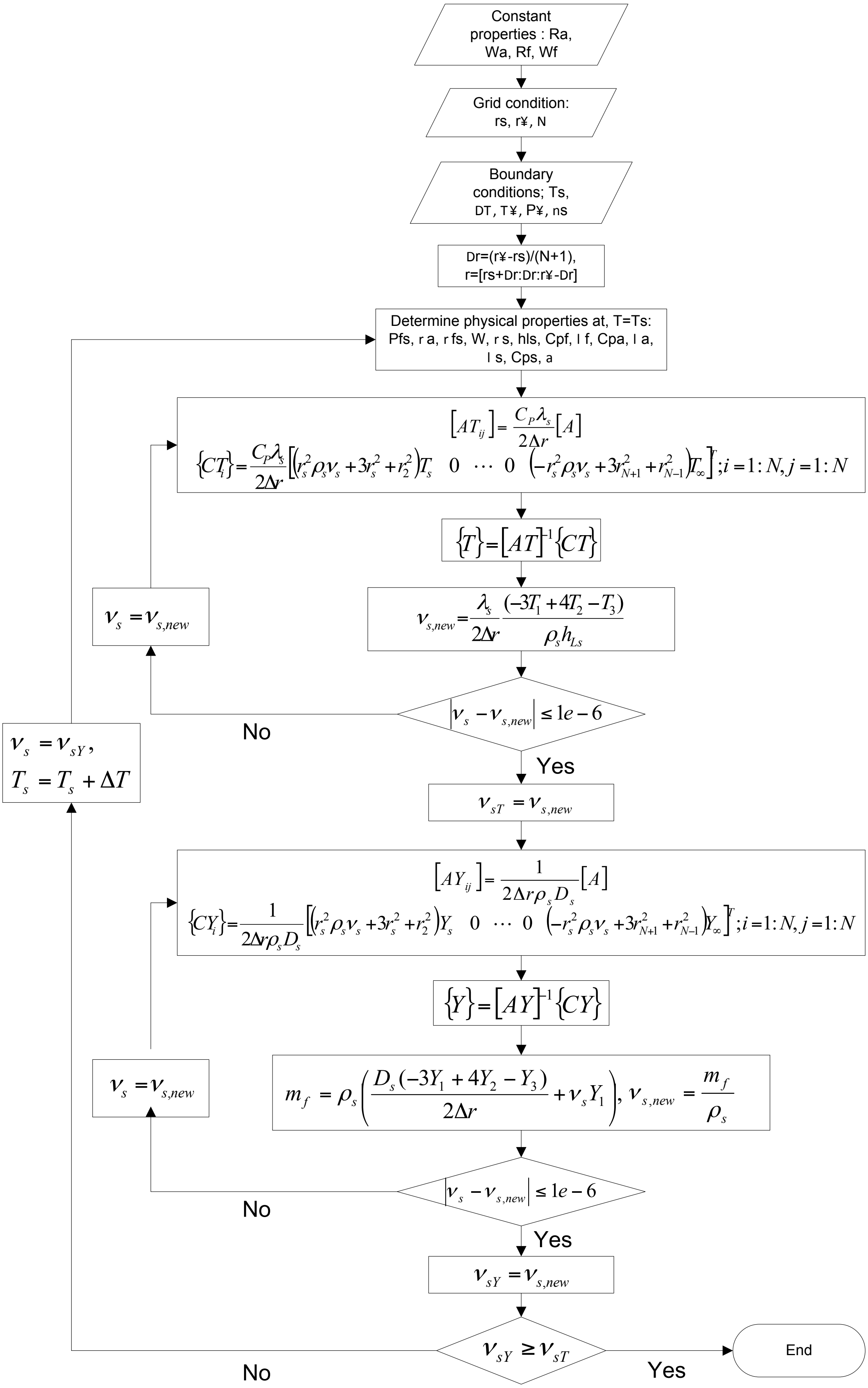
Constant properties : Ra, Wa, Rf, Wf
Grid condition: rs, r¥, N
Boundary conditions; Ts, DT, T¥, P¥, ns
Dr=(r¥-rs)/(N+1), r=[rs+Dr:Dr:r¥-Dr]
Determine physical properties at, T=Ts: Pfs, r a, r fs, W, r s, hls, Cpf, l f, Cpa, l a, l s, Cps, a
$\left[AT_{ij}\right]=\frac{C_P\lambda_s}{2\Delta r}[A]$
$\{CT_i\}=\frac{C_P\lambda_s}{2\Delta r}\left[\left(r_s^2\rho_s v_s+3r_s^2+r_2^2\right)T_s \quad 0 \quad \cdots \quad 0 \quad \left(-r_s^2\rho_s v_s+3r_{N+1}^2+r_{N-1}^2\right)T_\infty\right]^T; i=1:N, j=1:N$
$\{T\}=[AT]^{-1}\{CT\}$
$v_{s,new}=\frac{\lambda_s}{2\Delta r}\frac{(-3T_1+4T_2-T_3)}{\rho_s h_{Ls}}$
$|v_s-v_{s,new}|\le 1e-6$
No
Yes
$v_s=v_{s,new}$
$v_{sT}=v_{s,new}$
$v_s=v_{sY},$
$T_s=T_s+\Delta T$
$\left[AY_{ij}\right]=\frac{1}{2\Delta r\rho_s D_s}[A]$
$\{CY_i\}=\frac{1}{2\Delta r\rho_s D_s}\left[\left(r_s^2\rho_s v_s+3r_s^2+r_2^2\right)Y_s \quad 0 \quad \cdots \quad 0 \quad \left(-r_s^2\rho_s v_s+3r_{N+1}^2+r_{N-1}^2\right)Y_\infty\right]^T; i=1:N, j=1:N$
$\{Y\}=[AY]^{-1}\{CY\}$
$m_f=\rho_s\left(\frac{D_s(-3Y_1+4Y_2-Y_3)}{2\Delta r}+v_sY_1\right), v_{s,new}=\frac{m_f}{\rho_s}$
$v_s=v_{s,new}$
$|v_s-v_{s,new}|\le 1e-6$
No
Yes
$v_{sY}=v_{s,new}$
$v_{sY}\ge v_{sT}$
No
Yes
End

where :

$$[A_{ij}]=\begin{bmatrix} 4r_s^2+4r_2^2 & r_s^2\rho_s v_s-r_s^2+3r_2^2 & 0 & 0 & \cdots & 0 & 0 & 0 & 0 \\ -r_s^2\rho_s v_s-3r_1^2+r_3^2 & 4r_1^2+4r_3^2 & r_s^2\rho_s v_s-r_1^2+3r_3^2 & 0 & \cdots & 0 & 0 & 0 & 0 \\ 0 & -r_s^2\rho_s v_s-3r_2^2+r_4^2 & 4r_2^2+4r_4^2 & r_s^2\rho_s v_s-r_1^2+3r_3^2 & \cdots & 0 & 0 & 0 & 0 \\ 0 & 0 & -r_s^2\rho_s v_s-3r_3^2+r_5^2 & 4r_3^2+4r_5^2 & \cdots & 0 & 0 & 0 & 0 \\ 0 & 0 & 0 & -r_s^2\rho_s v_s-3r_4^2+r_6^2 & \cdots & 0 & 0 & 0 & 0 \\ \vdots & \vdots & \vdots & \vdots & \ddots & \vdots & \vdots & \vdots & \vdots \\ 0 & 0 & 0 & 0 & \cdots & -r_s^2\rho_s v_s-3r_j^2+r_{j+2}^2 & 4r_{j-1}^2+4r_{j+1}^2 & r_s^2\rho_s v_s-r_{j-2}^2+3r_\infty^2 & 0 \\ 0 & 0 & 0 & 0 & \cdots & 0 & -r_s^2\rho_s v_s-3r_j^2+r_{j+2}^2 & 4r_{j-1}^2+4r_{j+1}^2 & r_s^2\rho_s v_s-r_{j-2}^2+3r_\infty^2 \\ 0 & 0 & 0 & 0 & \cdots & 0 & 0 & -r_s^2\rho_s v_s-3r_{N-1}^2+r_\infty^2 & 4r_{N-1}^2+4r_\infty^2 \end{bmatrix}$$

With this method, the evaporation rate of a liquid is estimated under the assumption of a constant diameter. We use this method to provide the solution, i.e. T_s, Y_{Fs} and mass flux $\rho_s v_s$, at the different diameter as the database. Then, the mass continuity equation is discretized with time to determine the drop diameter at each time step as;

$$\rho_l \frac{d(\pi D^3/6)}{dt} = -\rho_s v_s \pi D^2$$

$$\rho_l \frac{\pi D^2}{2}\frac{dD}{dt} = -\rho_s v_s \pi D^2$$

$$\frac{D_{i+1} - D_i}{\Delta t} = \frac{-2\rho_{s_i} v_{s_i}}{\rho_l}$$

$$D_{i+1} = D_i - \frac{2\rho_{s_i} v_{s_i}}{\rho_l}\Delta t$$

2.2 Rainbow Technique

The Rainbow Technique is a non –intrusive technique that utilizes the interaction of the light experimenting one internal reflection inside the droplet. As schematized in Fig. 2.3, when the light impinges on the drop surface, some parts of it reflect and some parts refract due to the change of the refractive index. The value of p indicates the number of chord along the light path inside the droplet. The first rainbow (p=2) appeared at the backward scattering angle is contributed from the interaction of the once internal reflected and twice refracted rays. The rainbow pattern is sensitive to the drop-size and the refractive index, where the latter is a function of temperature. As schematized in Fig. 2.4, the main rainbow and supernumerary bows, the lower frequency, are created by the interference between the rays with one internal reflection. The ripple structure, the higher frequency, is formed by the interference between the light externally reflected (p=0) and the internal reflected light (p=2). Alexander dark band separates the first rainbow from the second rainbow.

Many theories have been introduced for the rainbow approximation. The transmission of the light impinging on a spherical drop can be explained by the geometrical optic, which applies Descartes-Snell’s Law. From the geometrical optic, the predicted rainbow position is directly dependent on refractive index but independent on drop size. Airy theory developed wave optics to predict rainbow position by taking drop size into account. The influence of drop size on the rainbow position is more significant in the smaller drop. The change in drop size causes a significant change in the angular distance between neighboring rainbow maxima. Therefore, the refractive index and drop size can be measured, according to Airy theory, by observing the rainbow position and the angular distance between supernumerary bows, respectively. However, the Airy prediction does not describe all the rainbow structure because the ripple structures are missing. For better accuracy, the Lorenz-Mie theory, which is the analytical solution to Maxwell Equation, is offered. The real rainbow structure can be computed from Lorenz-Mie theory but very time consuming. Nussenzveig theory [25] becomes the effective approximation. It has been proved that it is as accurate as Lorenz-Mie theory but computing as fast as Airy theory [15].

The previously described technique used for the single drop is called Standard Rainbow Technique (SRT). For spray characterization, the Global Rainbow Technique (GRT) is used. This technique is based on the same physical principle as the Standard Rainbow Technique. Nevertheless, the global rainbow pattern is created by the light scattered from a large number of particles. The ripple structure disappears because of the integration of the number of rainbow patterns. The global rainbow pattern is characterized by the main peak and followed by a tail. The main peak position and its shape depend, respectively, on the refractive index and size distribution. The examples of the rainbow image and the intensity distribution of the global rainbow from the work of Saengkaew [16] are shown in Fig. 2.5. In her work, the inversion algorithm to extract drop size distribution and refractive index of the liquid spray from the global rainbow signal has been developed based on Nussenzveig Theory because this theory is linear and the computation are very fast.

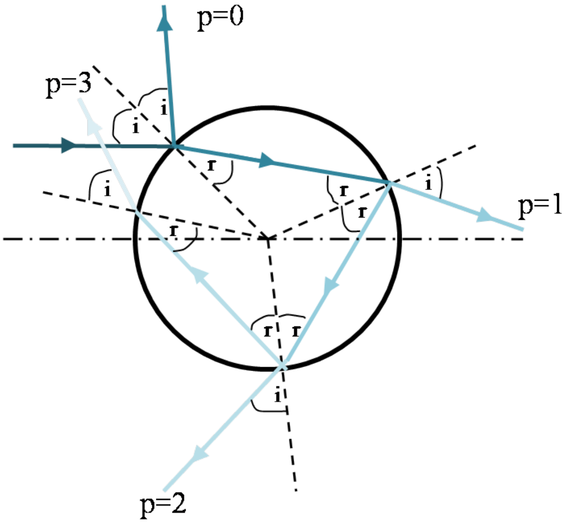

Figure 2.3: The illustration of the rays reflected and refracted from spherical drop, p present at the time that the ray transverses inside the droplet

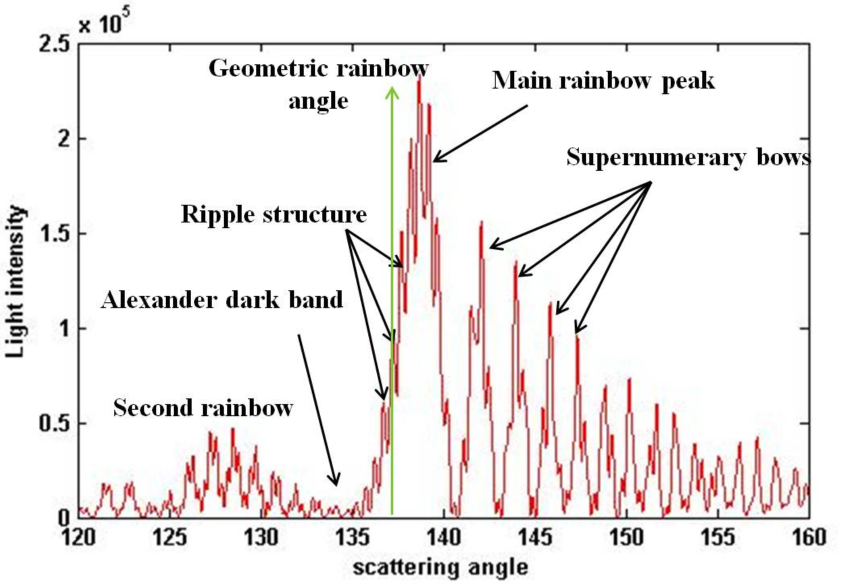

Figure 2.4: The backward scattering diagram

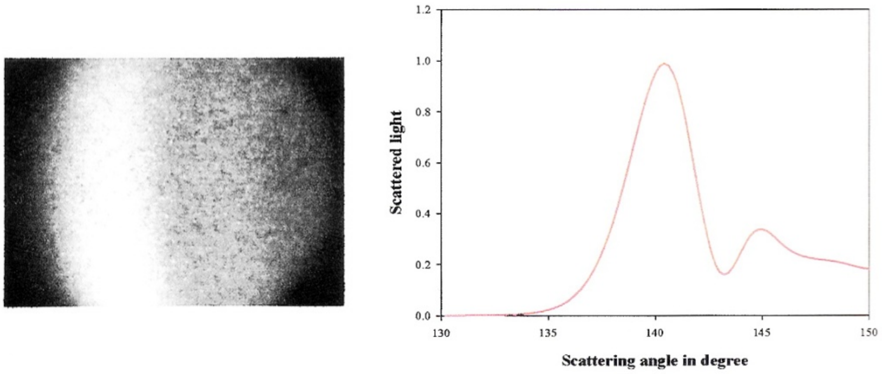

Figure 2.5: The global rainbow pattern scattered from water spray and the intensity distribution [16]

2.2.1 Rainbow Characteristics

As mentioned above, the rainbow characteristics mainly depend on two properties of the droplet, i.e. diameter and refractive index, where the droplet was assumed to be a perfect sphere. Fig. 2.6 shows the rainbow patterns simulated from calculation program based on Lorenz-Mie theory at three different refractive indices. The effect of the refractive index on the rainbow pattern is illustrated. An increase in the refractive index causes the rainbow pattern to shift to the larger scattering angle. The plot of the refractive index against the rainbow angle, which is predicted from the prediction program of rainbows by Nussenzveig approach, is shown in Fig. 2.7. The rainbow angle changes 1^{o} when the refractive index changes only 0.0074.

The drop diameter strongly affects the distance between the supernumerary bows. As shown in Fig. 2.8, the distances between the supernumerary bows are smaller when the droplet is larger. For the tiny change of diameter, the change of main peak and the supernumerary bow cannot be detected but the movement of the ripple structure can be observed instead.

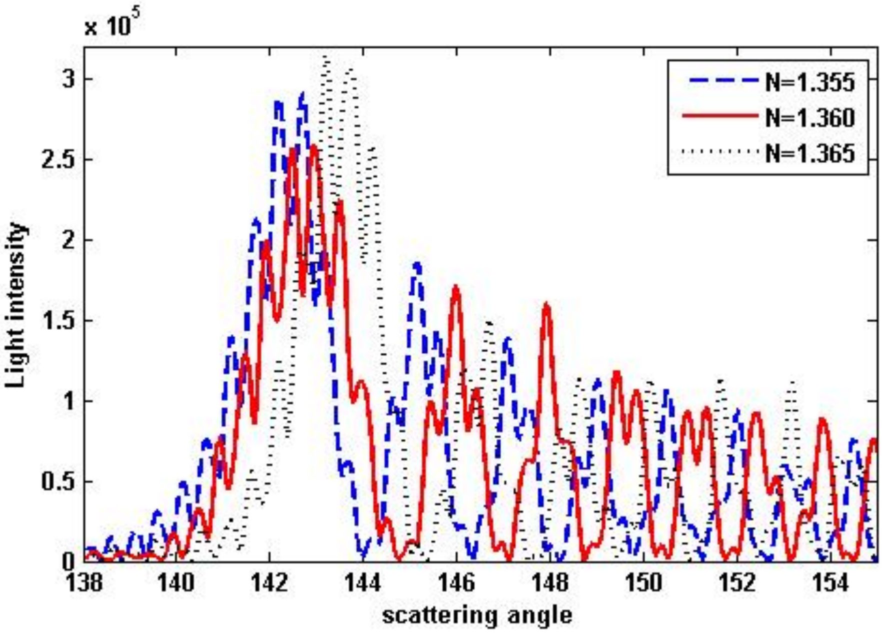

Figure 2.6: The rainbow simulation of 100 -µm droplet at different refractive indexes

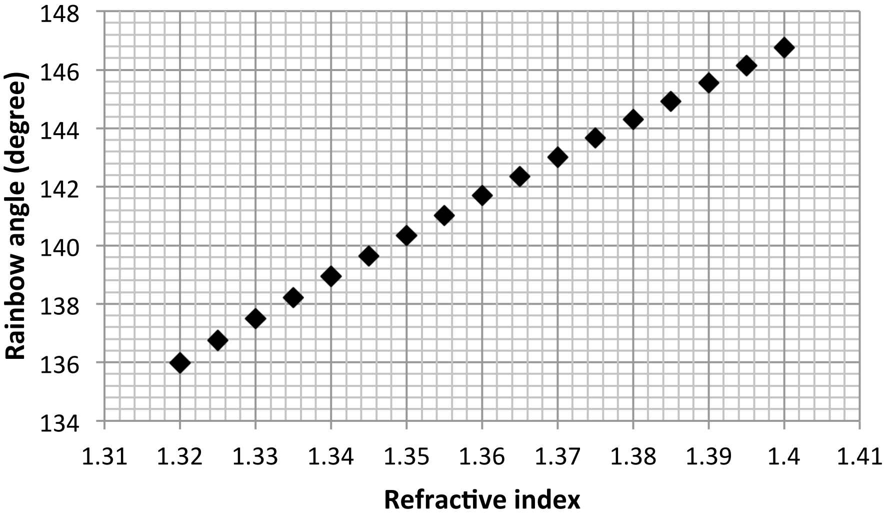

Figure 2.7: The rainbow angle plotted against the refractive index obtained from the rainbow prediction program based on Nussenzveig theory.

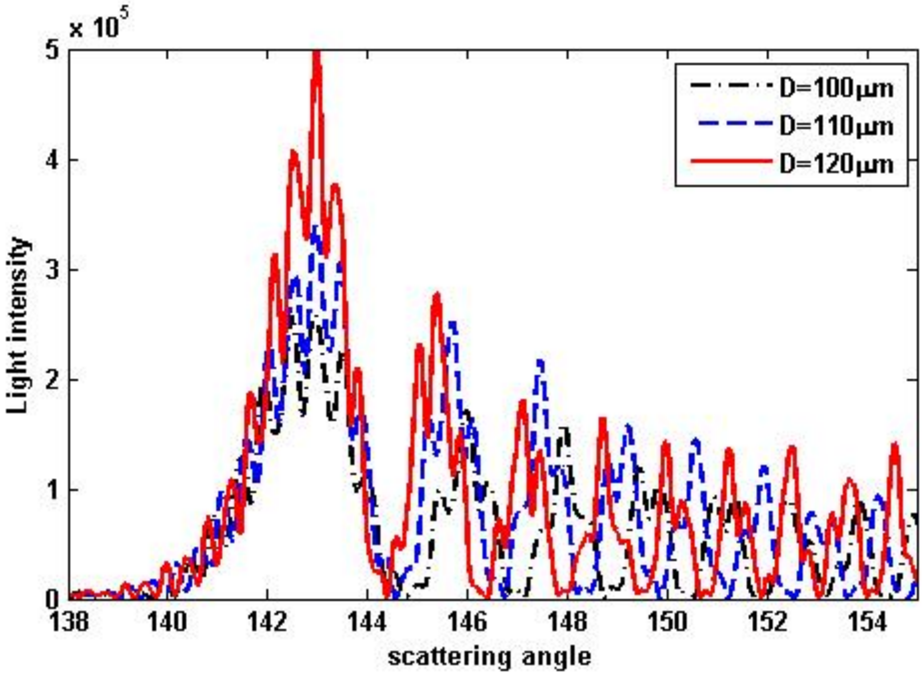

Figure 2.8: The simulated rainbow of the droplet whose refractive index equals 1.3600 at different diameters

2.2.2 Global Rainbow Setup

An effective GRT setup was designed by Saengkaew S. [16]. The experimental set-up mainly consists of the laser as the emitter and the optical system as the receiver. The receiving part for GRT consists of a system of lens and pinhole as schematized in Fig. 2.9. The scattered light is collected and focused by the first lens while the second lens conjugates the rainbow pattern at the focal plane of the first lens, in which the scattered light impinging on the first lens at the same angle are located at the same position, onto the screen at the image plane. Between the two lenses, at the image plane of the first lens, the pinhole is installed to block the unwanted light from outside the measurement volume. The angle between laser and optic line should be about the rainbow angle of the liquid. With this set up, only the light scattered from the droplets in the measurement volume around the desired angle can be collected.

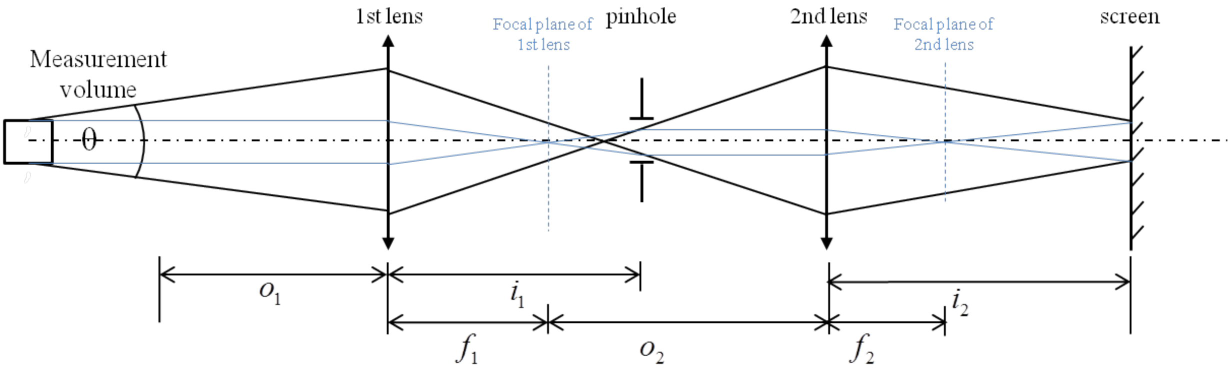

Figure 2.9: The alignment of the optical system for the receiving part

The position of the lenses and the pinhole can be adjusted to a specified measurement volume and scattering angle. The position of each component can be calculated by using the geometry of lens. This section shows the calculation of the position of each component and the corresponding measurement volume and the collected scattering angle. Recalling Fig. 2.9, f_1, D_1 and f_2, D_2 refer to the focal length and diameter of the first lens and second lens, respectively. Assuming that the lenses used in the experiment are thin lens, the image plane, which is the distance from 1st lens to pinhole, i_1, and from 2nd lens to screen, i_2, can be calculated by using the equation below;

$$i_j = \frac{f_j o_j}{f_j - o_j}; j = 1,2.$$

The solid collection angle, θ, that can be collected by the 1st lens is;

$$\theta = 2\tan^{-1}\left(\frac{D_1/2}{o_1}\right).$$

The relationship between the width of the measurement volume, d_m, and the diameter of the pinhole, d_p, is:

$$d_p = d_m\left(\frac{f_1}{f_1 - o_1}\right)$$

CHAPTER 3
EVAPORATION OF AN INDIVIDUAL DROPLET

In order to understand the evaporation behavior of the liquid drop, the evaporation of a single droplet is observed. Since a spray can be considered as the integration of a number of single droplets, the evaporation of an individual droplet is still interesting. This chapter presents the experimental study of the evaporation of a suspended individual droplet. Section 3.1 describes the measurement of the size and refractive index of the ethanol droplet in the still air by using rainbow and imaging techniques. Water and ethanol are the liquid used in this study. The results and discussions are presented in section 3.2.

3.1 The Measurement of Size and Refractive Index

To understand the evaporation behavior of a liquid droplet, the diameter and temperature are very useful parameters. The diameter change allows us to calculate the mass flux transfer through the drop surface while the drop temperature leads us to an estimation of the physical properties of fuel vapor. In this research, we use the imaging technique to monitor the size and shape of the droplet. The refractive index, which depends on the temperature, is extracted from the rainbow signal. The experimental set-up and calibration are detailed in the Sections 3.1.1 and 3.1.2, respectively. Airy theory was used in an inversion process to extract the diameter and refractive index of the droplet from the rainbow signal, which is denoted in Section 3.1.3.

3.1.1 Experimental Setup

The experimental setup of two measurement techniques, namely shadow imaging and rainbow technique, were developed. The first technique measures the size and the latter measures both the size and the refractive index of the evaporating droplet. The experimental setup consists of three main parts, i.e. laser emitter, liquid droplet and image receivers. Measurements with the two techniques are carried out simultaneously. The complete setup is shown in Fig. 3.1.

For the shadow imaging technique, the light source used was a red backlight. The liquid drop is initially created by a syringe-needle then suspended on the well-fixed optical fiber. A CCD-camera connected with a macro lens, called camera-1, is used to capture the shadow image of the droplet. Camera-1 is marked by a magenta filter to allow mostly the red light to pass and being set perpendicular to the laser beam, to minimize the irradiation of the scattered green laser light from the other measurement.

A green light source of 532-nm wavelength and 100 mW power is used for the Rainbow Technique. The laser diameter at the aperture is 2 mm. The optical train of the receiving part consisted of a plano-convex lens with 30 cm focal length and a screen placed at the focal plane behind the lens. At the end of train, a 480×512 pixel^2 –CCD camera from Keyence (Model: CV-H035M), named camera-2, together with a green filter are setup to receive the rainbow signal projected on the screen. Since the screen is located at the focal plane of lens, all light that scatter at the same angle will be focused on the same point on the screen even though it comes from the different position. Both camera-1 and -2 are connected to the same controller for simultaneous recording.

The experiments are conducted with two liquids, water and ethanol, at room temperature and atmospheric pressure. The temperature and relative humidity of the surrounding are measured by a digital temperature-relative humidity meter (DIGICON HT-770). The accuracies of the temperature and the relative humidity measurement are within 0.1°C and 5% respectively. For the water droplet, a 125 -µm optical fiber is used as the suspender. In case of ethanol, three sizes of optical fiber (125, 250 and 400 µm) are used to compare the effect of the size of drop suspender. An experiment without laser is also conducted to investigate the effect of the laser on the evaporation rate; in this case only the imaging technique being available. The experiments are repeated three times for each size of suspender, with and without laser. The initial drop diameter is around 1.2-1.8 mm and is not the same for each experiment.

3.1.2 Calibration

Calibration is the most important process for this experiment as it directly affects the accuracy of the measurement results. For the shadow imaging technique, the calibration is carried out to determine the magnification of the camera. In parallel, the pixel position of another camera is correlated with the scattering angle.

- <u>Camera for imaging technique</u>

A concentric circle reticle is used for the calibration. It consists of a centered crosshair and ten concentric circles, each spaced 1 mm apart, formed from the lines of 25 μm wide, as shown in Figure 3.2. The space between each circle is measured from the image in the pixel. Hence, the correlation between pixel and real distance (in mm) can be determined. In this case, the calibration result gives a pixel equal to 14 μm. Thus, the accuracy of this technique is 7 μm.

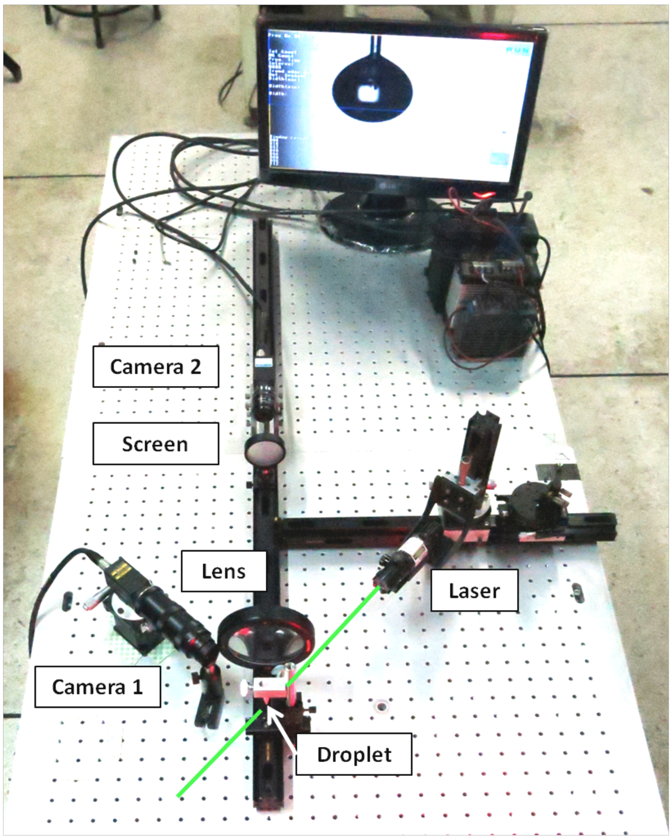

Figure 3.1: The experimental setup

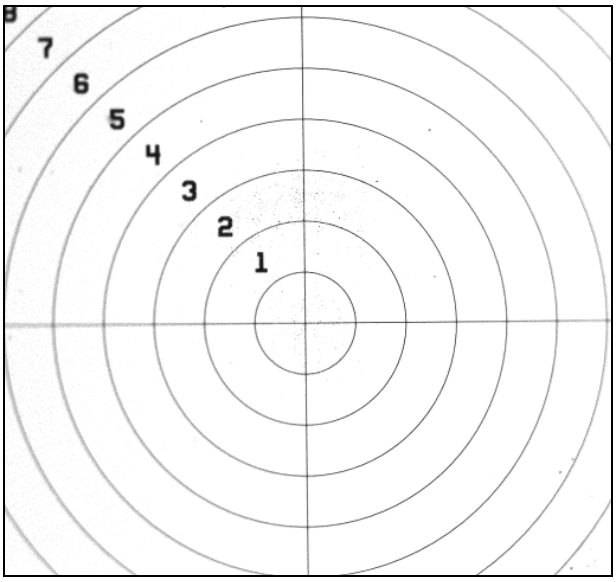

Figure 3.2: Image of the concentric circle reticle used in the calibration. This image gives a pixel = 14 μm.

- Camera for rainbow technique

The calibration is employed before the experiment to find the angle position of each pixel of the camera. The reflection mirror is used in the calibration. It is located at the position where the droplet is placed. The scattering angle is the angle of the reflected light referred to as the forward laser beam, which can be determined from the angle of the mirror as demonstrated in Fig. 3.3. To enable the mirror to be rotated in a very small and accurate angle, the mirror is installed on a fine adjustable rotator. When rotating the mirror in a small angle, the position of the reflected light appeared on the pixel of the camera changes.

Fig. 3.4 shows the images of the reflected light when the mirror by is rotated in 0.2° steps. Then, the relation between scattering angle and pixel position can be determined from the linear regression of the plot of the scattering angle versus pixel position as shown in Fig. 3.5. The relations of the pixel position and scattering angle for the water droplet and ethanol droplet are:

water: angle = -0.004847*pixel + 140.05,

ethanol: angle = -0.01198*pixel + 145.50.

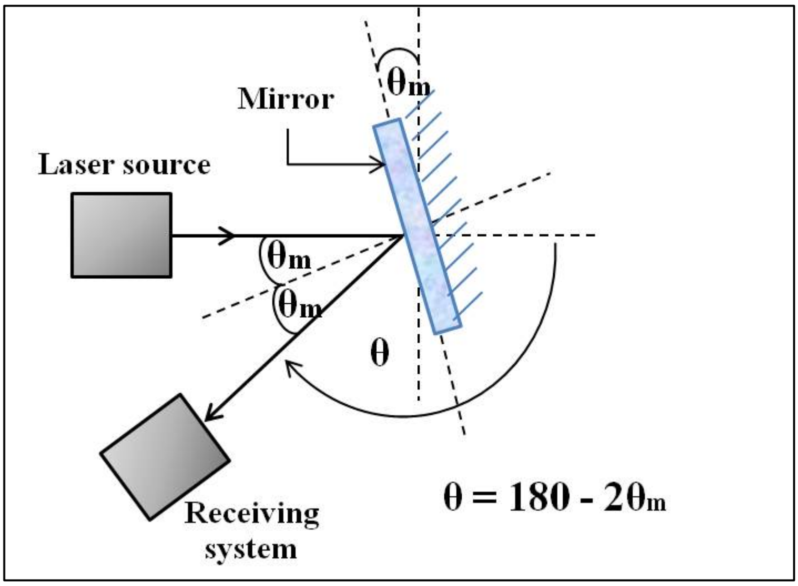

Figure 3.3: The illustration of mirror calibration

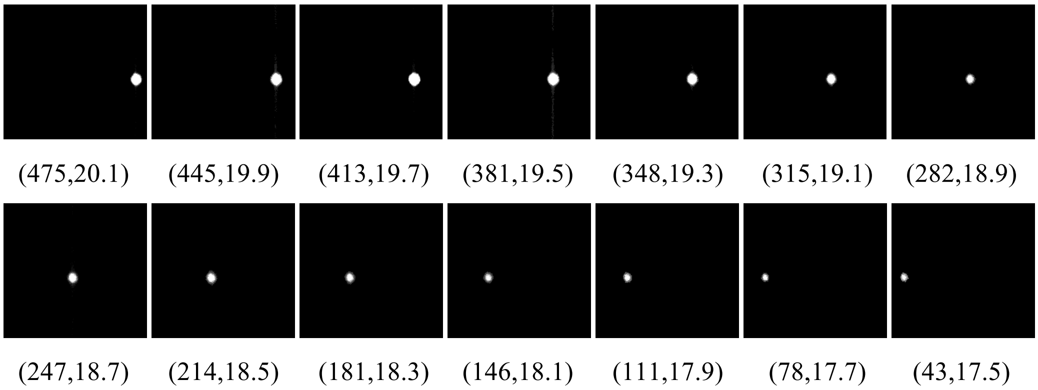
(475,20.1) (445,19.9) (413,19.7) (381,19.5) (348,19.3) (315,19.1) (282,18.9)

(247,18.7) (214,18.5) (181,18.3) (146,18.1) (111,17.9) (78,17.7) (43,17.5)

Figure 3.4: The recorded reflected light during the calibration. The number under the image is the coordinate pair of the pixel's position and angle of the mirror, (pixel, θ_m).

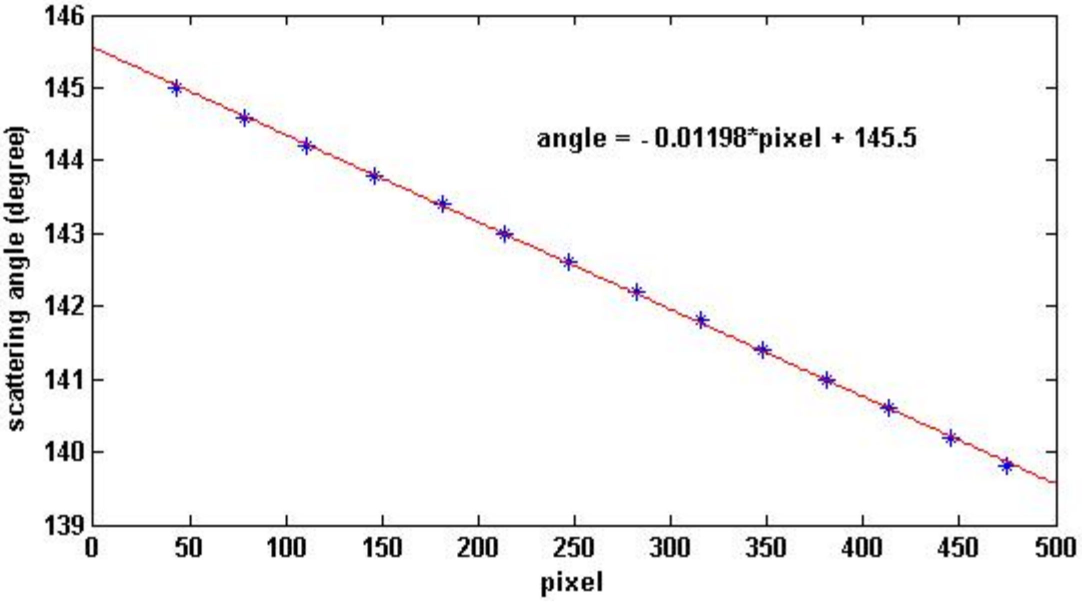

Figure 3.5: The plot of the pixel position versus the scattering angle, $\theta = 180 - 2\theta_m$, for the ethanol measurement

3.1.3 Image Processing

The drop diameter can be measured from the recorded drop image. Edge detection is performed on the shadow image, and the maximum length between the two edges in the horizontal direction is taken as the diameter of the droplet, as shown in Fig. 3.6. The accuracy of the measured diameter is delimited by the width of the pixel, which is equal to 14 μm for the current setup.

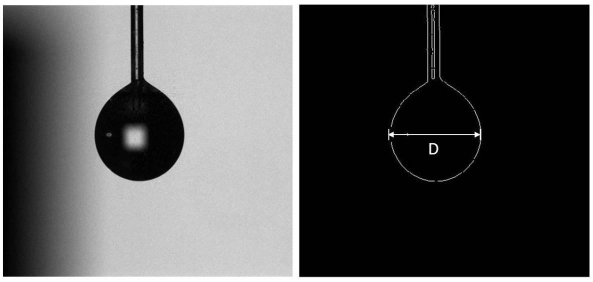

Figure 3.6: The shadow image of the droplet (left) and the filtered image (right) for the diameter measurement

Image processing is carried out to extract the refractive index of the droplet. A Matlab code for image processing is written and works by the following steps:

- Read an image as a matrix where the value of each element is the intensity of each pixel in the ith column and the jth line. In this case, size of matrix is 480×512, corresponding to the number of pixel of the camera.
- Select the integration zone which is the 5 lines where the curvature of the rainbow signal is tangent to the vertical line, as demonstrated in Figure 3.7.
- Average the intensity along the column and transform the pixel to the angle by using the relation from the calibration. Now, the vector of light intensity on the scattering angle, $I(\theta)$, is obtained.
- Normalize the intensity by the maximum intensity and filter the signal to manage the noise and the high frequency signal. For the droplet in the millimeter scale, the amplitude of the main peaks and the supernumerary is much larger than that of the noise and the ripple structure (the high frequency signal). So that the effect of the filtering process on the accuracy of the extracted results is ignored.
- Fit the filtered signal with the Airy Equation, which is reviewed in Appendix A, extract the refractive index by using the least-squared method. The plot of the original and the filtered signals with their best fit to the Airy Equation can be seen in Fig. 3.8.

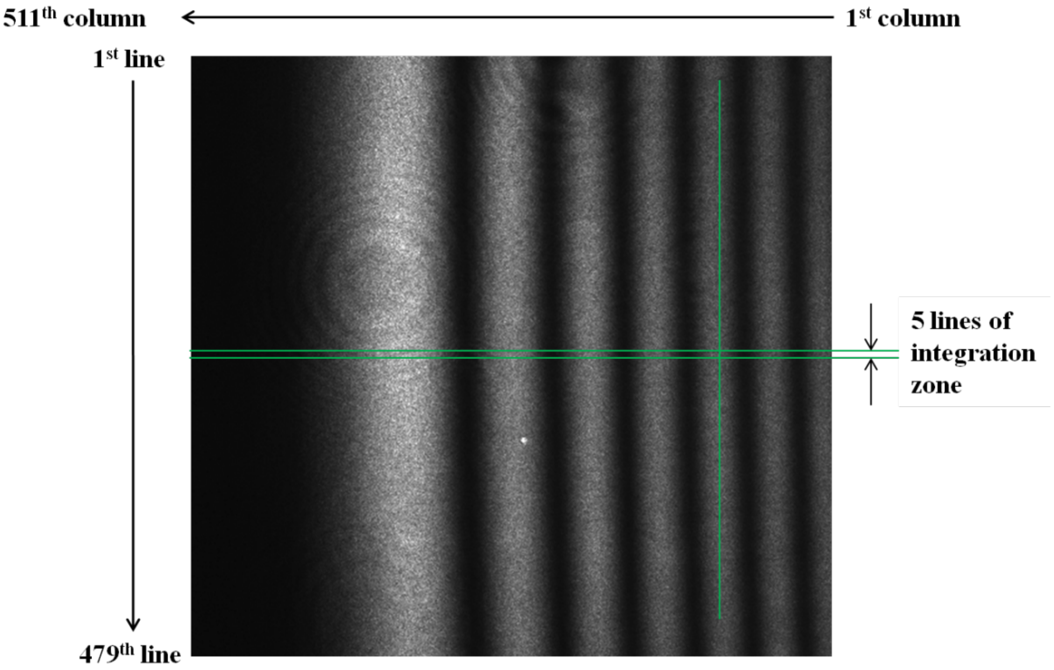

Figure 3.7: The selection of integration zone for the inversion process

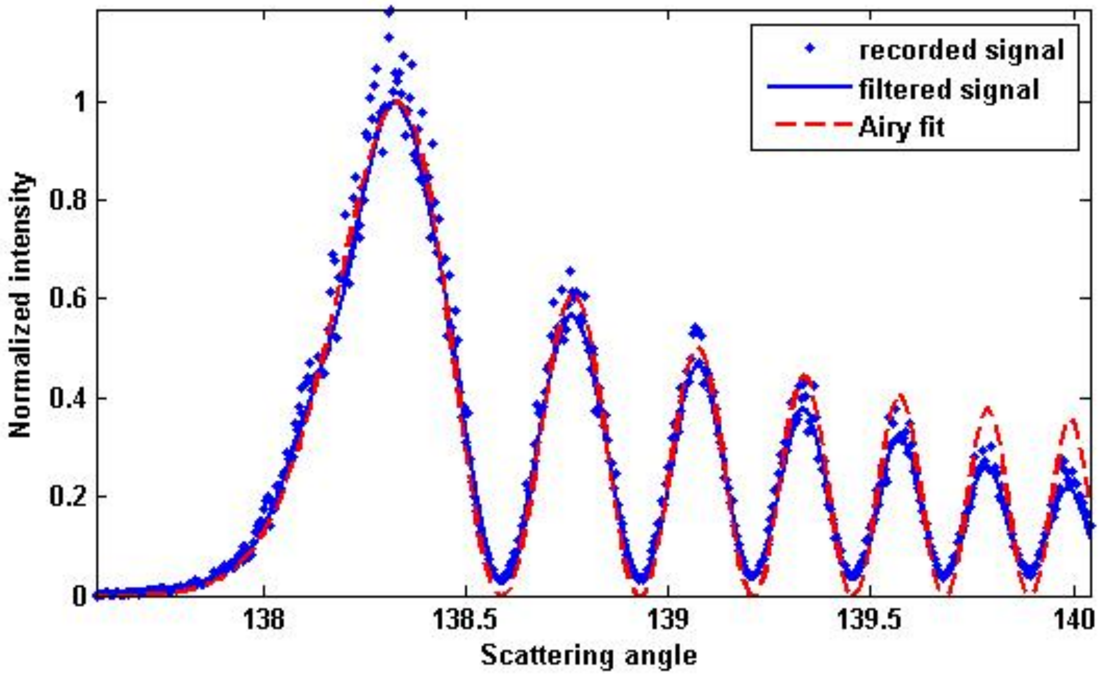

Figure 3.8: The original and filtered rainbow signals with their best fit to the Airy Equation

3.2 Results and Discussion

3.2.1 Water

Five sets of experiments were carried out. In the experiment, the water droplet is left to evaporate under room temperature. The sampling rate is 2 images per second at the first 1 minute from the beginning. After that, the sampling rate is reduced to 1/120 images per second. The laser light illuminates on the droplet only 5-10 seconds during which the image is taken. The effect of laser power is ignored. The plot of D^2 versus time of the evaporating droplet at an ambient temperature of 28.6 ^{o}C is shown to be a linear function following the D^2-law, the classical evaporation theory (see Fig. 3.9). With the linear regression model being fit to the experimental data, the slope of the regression is called evaporation constant, *β*, of the evaporated liquid droplet. For this particular experimental test case, it is found that the evaporation constant is equal to 5.47×10^{-4} mm^2/s. The D^2-t relation is used as the template for evaluating the surface temperature of the droplet and the humidity ratio of the ambient moist air.

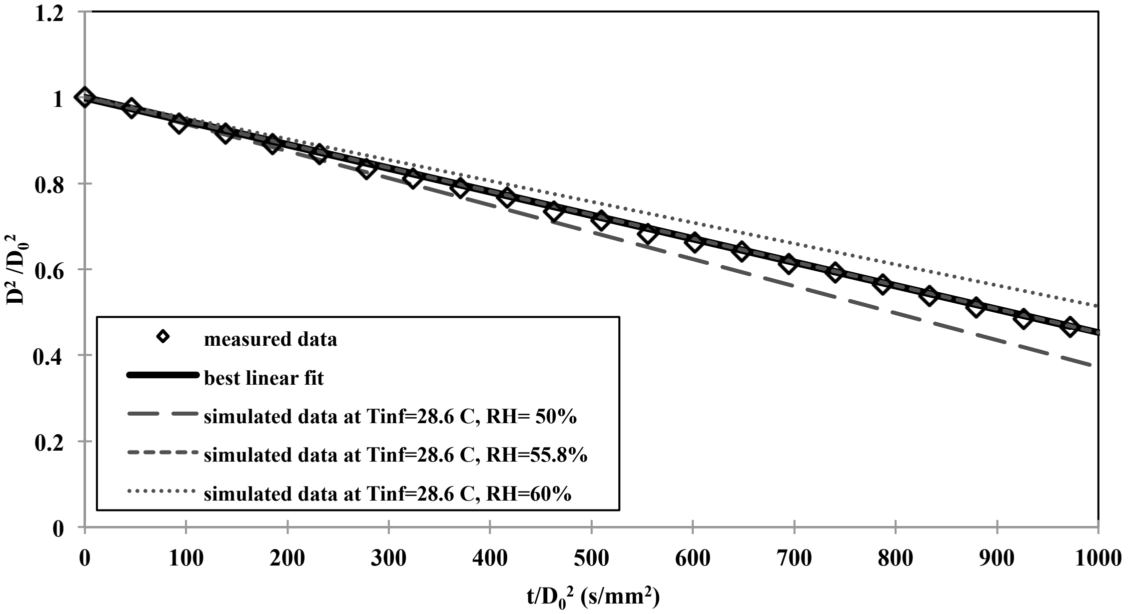

Figure 3.9: D^2-t plot of the drop evaporating in the surrounding air temperature, $T_\infty = 28.6^o$C; the slope or the evaporation constant being 5.47×10^{-4} mm^2/s. At the same surrounding air temperature, the optimized value of humidity is 55.8%.

The curve of D^2-t is resolved by using the evaporative model presented in Section 2.1.3. To solve the numerical problem, the humidity ratio at the outer boundary is changed iteratively until the regression of D^2-t plot obtained from the model coincide with that obtained from the image analyses, which is demonstrated in Fig. 3.9. The relative humidity obtained from the model, RH_{model}, is found to be 55.8% and the surface temperature of the droplet, $T_{s,model}$, 22°C. The two properties are in accordance with the relative humidity and the adiabatic saturation temperature of the surrounding moist air respectively.

To obtain the temperature and relative humidity experimentally and independently, the surface temperature, $T_{s,rb}$, is measured by the Rainbow Technique and the relative humidity, RH_{psy}, by a psychrometer. Their measured values are 23°C and 59.5% respectively. The results obtained from the two measurement methods are in very good agreement with those obtained from the imaging technique together with the evaporation model.

Water, with its temperature being lower than the wet bulb temperature of the ambient air, is used to make a suspended droplet. The rainbow signal appears on the screen as interference fringes. The fringes are read into a matrix form, on the pixels of camera-2 as depicted in Fig. 3.10 (left). The pixel position on a selected row is calibrated into angular position. As can be seen from the horizontal axis of the horizontal axis of graph in Fig.3.10 (right), the angular position spans about 3°. It can be remarked that since the screen is located at the focal plane of lens, all scattered light from the droplet of the same angle have been focused onto the same point on the screen even though they come from different position.

Before the experiment, the water temperature was set at 0°C. During the sensible heating of the droplet, the measured refractive index, N, varied from 1.33542 to 1.33491. Thereafter the droplet evaporated and the value of Noscillated about the value at the upper limit (N=1.33491), as plotted in Fig 3.11. The refractive index of the liquid relates directly to its temperature, the relations between them being given by P. Schiebener and J. Strab [26], see details in Appendix B. The droplet temperature, transformed from the measured refractive index of droplet, is shown in Fig. 3.12. It can be seen that during sensible heating the temperature of the droplet rises; that is in agreement with the experiment results of A. Fujita, et. al. [27]. When the temperature of the droplet reaches adiabatic saturation temperature, the heat transfer to the droplet transforms into latent heating. At this state the droplet is saturated water with evaporation occurring at its surface. The measurement results confirm the assumption of the constant temperature of the droplet. It can be also implied that the temperature inside droplet is uniform. The measured temperature oscillates about the mean temperature at 19.3°C with a root mean square error of 0.586°C. One of the main causes of this sway in temperature is the oscillatory nature of the suspended droplet, which is in turn due to the fact that the droplet suspender is connected directly to the optical bench without any vibration absorber. The precision of the refractive index measurement is, however, up to the fourth decimal place.

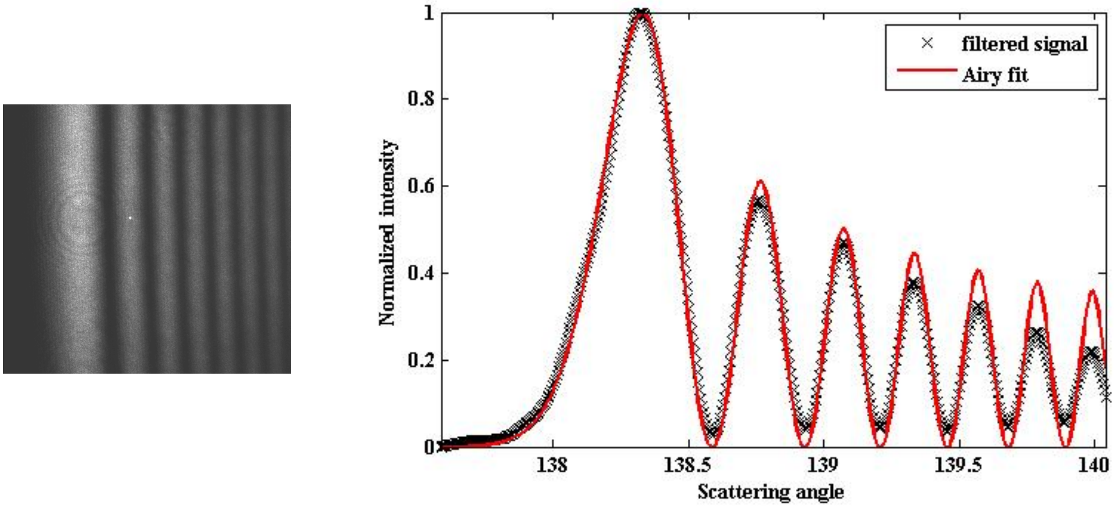

Figure 3.10: The images of the rainbow signals (left) and the radial distribution of the rainbow signal before and after filtering, and its best fit with the Airy Theory (right)

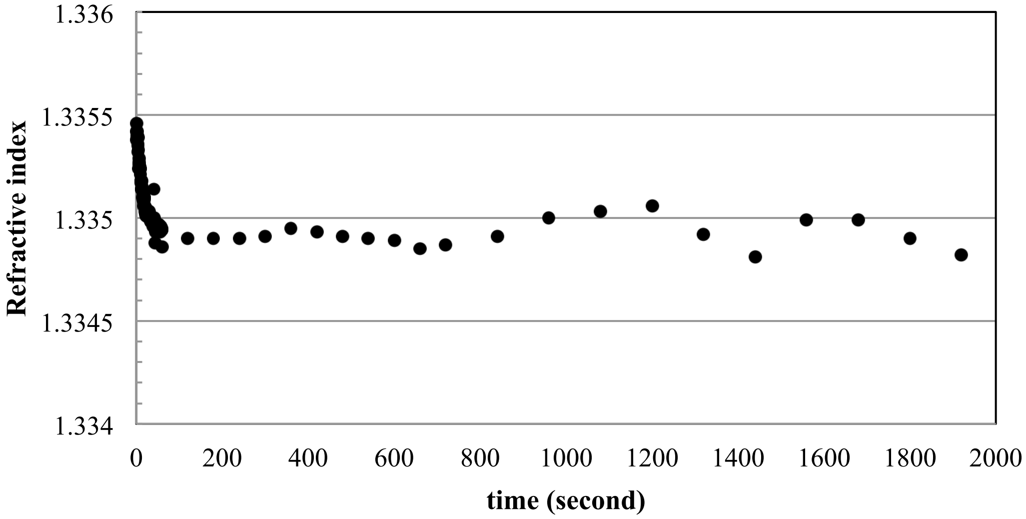

Figure 3.11: The history of the measured refractive indexes of water drop evaporated in the air at 27.3°C

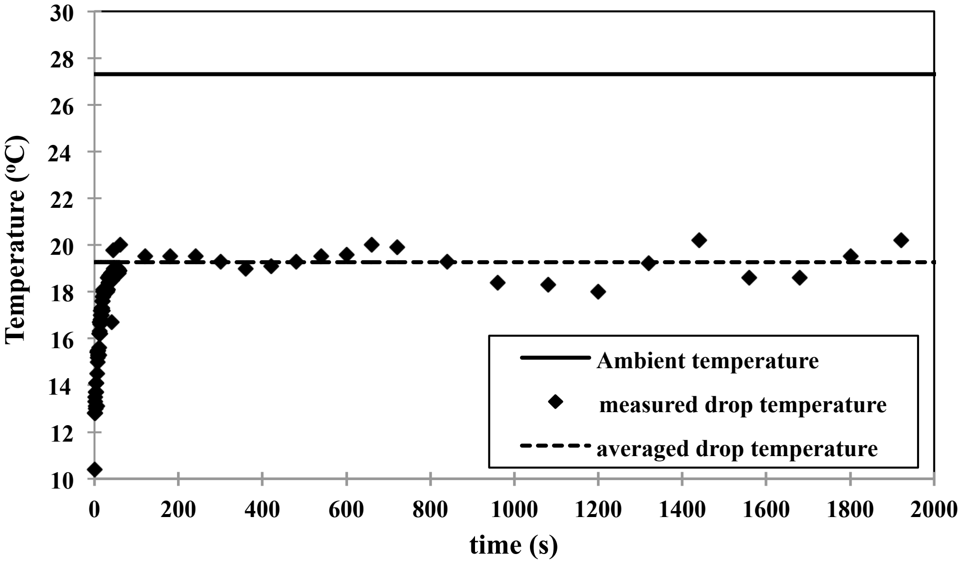

Figure 3.12: The temperature of water drop corresponding to the measured refractive index in Fig. 3.11.

Table 3.1 summarizes the droplet evaporation constant, and the simulated and measured droplet surface temperatures and relative humidities under five different ambient temperature conditions, using the techniques mentioned earlier. For all cases, the surface temperature and the relative humidity obtained from different measurement techniques are in good agreement. The error of the temperature is lower than 6%.

Table 3.1: The experimental condition and the measurement results

Drop No.	T_∞ ^oC	$\beta \times 10^4$ mm^2/s	$T_{s,model}$ ^oC	RH_{model} %	$T_{s,rb}$ ^oC	RH_{psy} %
1	26.7	4.33	21.6	63.1	21.3	67.2
2	27.4	6.42	19.7	47.5	18.6	49.6
3	28.2	4.42	22.9	63.2	22.7	66.1
4	28.6	5.47	22.0	55.8	23.0	59.5
5	29.2	4.83	22.4	62.3	21.7	62.3

3.3.2 Ethanol

The recorded images of a droplet suspended on three sizes of fiber optic, with and without using a laser are shown in Fig. 3.13. Three repetitions are carried out for each measurement condition. In case of the experiment with laser, the laser is turned on continuously during the imaging. The work of Haitao Yu et. al. [28] reveals that the rainbow pattern from the spheroidal droplet with the Airy theory can be used in the droplet characterization. Then, the deflection of droplet from the sphere due to the effect of the suspender is ignored. The initial size of droplet increases with the increase of the size of the suspender. Because of the surface tension, the droplet cannot be held at the tip of suspender but it stand on the length of the suspender. Therefore, the effect of the suspender must be considered.

	$D_{suspender}$=125 μm	$D_{suspender}$=250 μm	$D_{suspender}$=400 μm
with laser	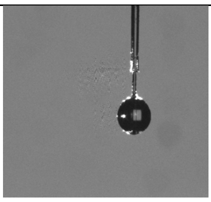	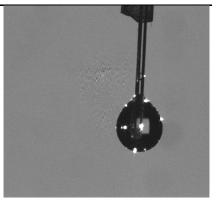	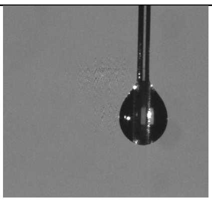
without laser	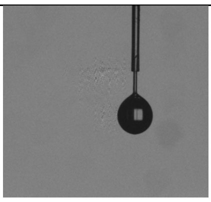	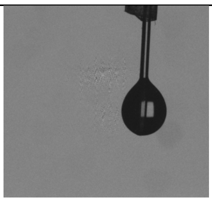	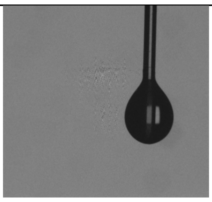

Figure 3.13: The shadow images of the initial droplet suspended on three sizes of fiber optic with and without laser

The measured drop diameters as a function of time are represented in Fig 3.14 for the fiber size 400 μm for with and without laser repeated three times. High degree repeatability of the experiments is found for every case of measurement. The plot shows the linear relation between diameter squared and time. The incidence of the laser light accelerates the evaporation rate of droplet. The linear regression is conducted to determine the evaporation constant, i.e. the average slope of the D^2-t plot. The evaporation constants as a function of fiber diameter squared are plotted in Fig 3.15. It can be seen that the evaporation constant linearly depends on the suspender diameter squared, which is in agreement with the work of Patrice [21]. Following his work, the evaporation rate of droplet without the suspender is determined by extrapolating the evaporation constant to where the fiber diameter is zero. From this method, the evaporation constants of ethanol droplet without suspender, with and without laser, are 0.0142 and 0.0109 mm^2/s, respectively. The calculated evaporation constant using the exact solution in Section 2.1.2 at the measurement condition being 0.0075 mm^2/s is underestimated.

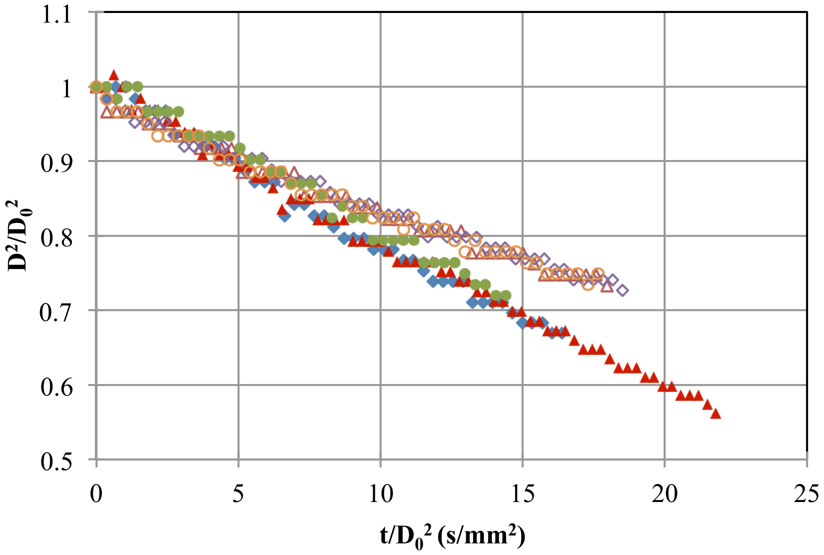

Figure 3.14: Drop size history for the drop suspended on the 400 μm diameter fiber optic in the case of presence (solid mark) and absence (light mark) of laser. The air temperature is 32.5±0.5°C.

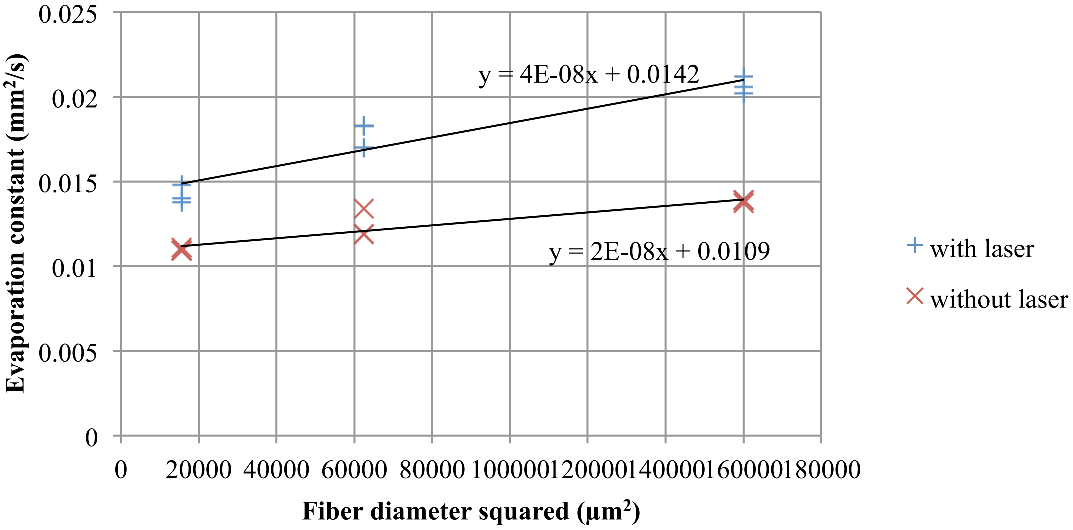

Figure 3.15: The evaporation constant of the droplet suspended on different sizes of fiber optic

The refractive index measured by the rainbow technique indicates the temperature of the droplet. The refractive index decreases when the liquid temperature increases. The diameter measurement results show that the laser light affects the evaporation rate of the liquid. However, it does not affect the surface temperature of droplet because that parameter is controlled by the ambient temperature and pressure. The histories of refractive index of the droplet are shown in Fig. 3.16. As can be seen, the refractive index increases continuously at the beginning, that is the temperature decreases. It is in agreement with the calculation result of the adiabatic saturation temperature, which is 2.8^{o}C, while the initial liquid temperature is about 30^{o}C. The same conclusion as the case of water droplet can be drawn.

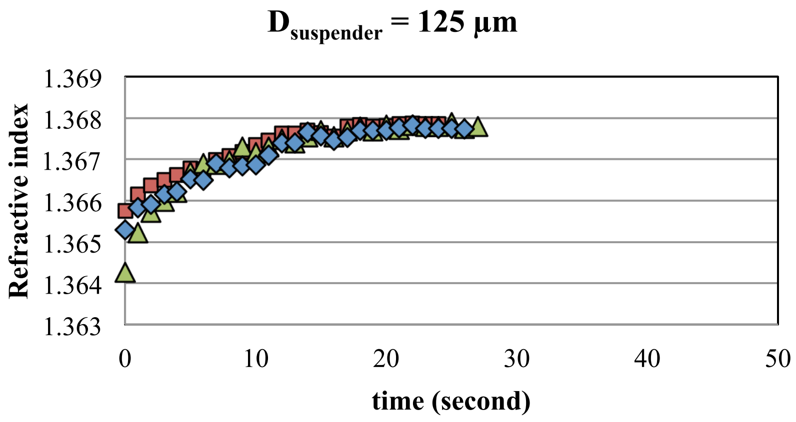

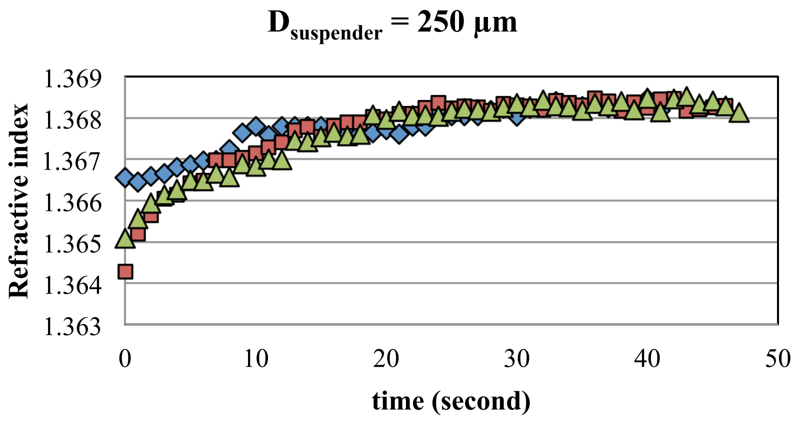

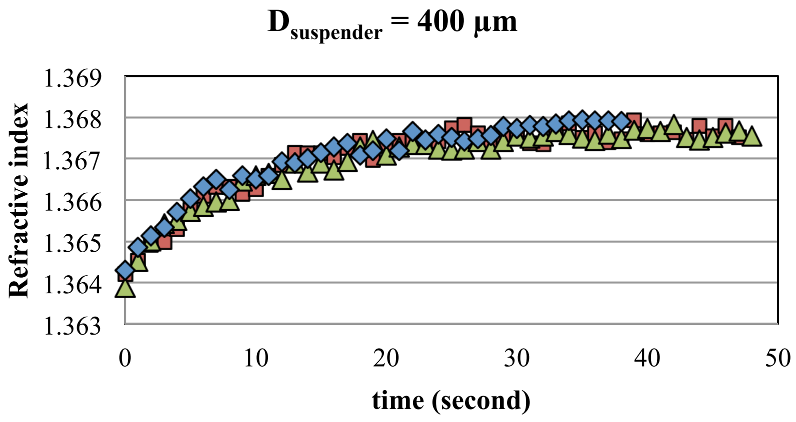

Figure 3.16: The measured refractive indexes of the ethanol droplet evaporated in 32.5±0.5°C ambient air with three times repetitions for each fiber optic size

CHAPTER 4
EVAPORATION OF DROPLETS

A study on the evaporation of a single drop enables us to have a better understanding of the phenomena of heat and mass transfer through the drop surface. To be closer to the realistic situation of fuel spray combustion, the evaporation of droplets in spray is considered. For this purpose a mono-disperse droplet generator, which generates fairly constant and predictable drop size, has been developed and used in many spray studies [20, 29-32]. To measure tiny size change, approaches based on the characteristics of the light scattered around the rainbow angle have the potential to measure both the temperature and size of droplets. Although very accurate size measurement can be carried out with standard rainbow technique when using appropriate signal processing [33] the accuracy is not sufficient to quantify evaporation rate as very tiny diameter change must be measured. Section 4.1 proposes a new strategy to measure the droplet temperature, size and size change with nanometric accuracy, which are in turn used to estimate the evaporation constant of the evaporating droplets. The experimental setup and methodology are presented in Section 4.2. The measurement results of ethanol are presented and discussed in Section 4.3.

4.1 One-Dimension Rainbow Technique (ORT)

The One-dimensional Rainbow Technique (ORT) has recently been introduced to measure the mean temperature and size distribution behavior along the line [34]. The technique is the modification of the classical Global Rainbow Technique (GRT), enabling it to make line measurements. In this research, ORT is used to measure the droplet diameter at different levels to calculate the evaporation rate. The experimental setup is similar to the work of Wu et. al. [34] but mono-disperse droplet is used instead of liquid spray. The concept and experimental setup is demonstrated in Fig. 4.1. The laser beam is transformed to the laser sheet by using the cylindrical lens. The laser sheet is vertical and coincide with a line of mono-disperse droplets. The setup of the optical train is the same as in the GRT, as explained in Section 2.2.2. The horizontal slit is added at the front of the 1st lens to collect the light scattered from droplets at the specified range of the vertical level. The second lens conjugates the rainbow pattern on the screen. Used with the mono-disperse drop generator, a number of droplets along the drop array is illuminated by the laser sheet. The ribbon of rainbow pattern appearing on the screen is a sequence of rainbow signal emanating from the droplet at different positions along the line. Therefore, in only one time measurement, size and refractive index of the droplets at different levels can be obtained.

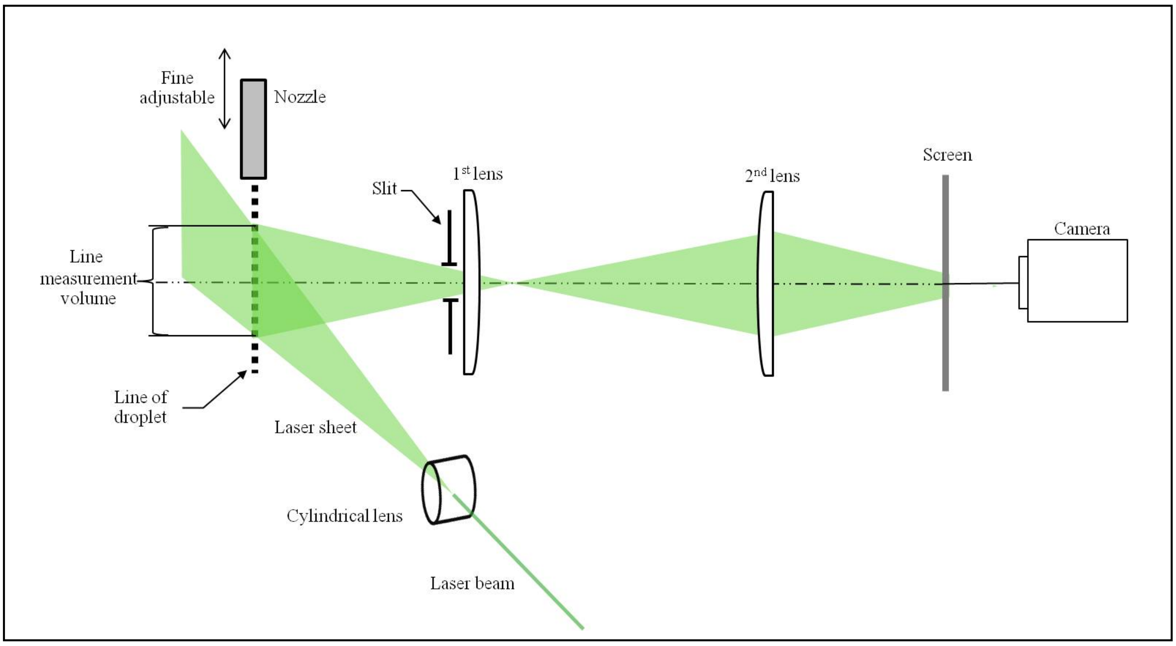

Figure 4.1: One-dimension Rainbow Technique setup

4.1.1 Rainbow Characteristics vs. Droplet Diameter

First of all, the effect of drop diameter to the rainbow signal is studied. The rainbow signal is simulated in the framework of the Lorenz-Mie Theory. The rainbow characteristic depends on two parameters, the drop diameter and the refractive index. The position of the rainbow (rainbow angle) depends on the refractive index while the distance between the low frequency peaks (supernumerary peaks) depends on the diameter of droplet; see the details in section 2.2. The high frequency or the ripple structure changes phase when the droplet diameter changes as small as 0.01 µm. Fig 4.2 shows the rainbow pattern simulated from the calculation program developed at CORIA based on the Lorenz-Mie theory for the refractive index N=1.3600 and the droplets of 99.90, 99.96, 100.02 and 100.08 μm diameter. It is found that if we keep increasing the drop diameter, the ripple phase will coincide with the initial diameter, for example, as in case of drop diameter 99.90 μm and 100.08 μm. This means that the correlation between the phase difference and diameter difference is a periodic function.

The rainbow signal is simulated based on the Lorenz-Mie Theory by varying diameter and refractive index. Since the droplet diameter used in the experiment is approximately 100 μm then drop diameter is varied from 99 μm to 101 μm with the increment by 0.01 μm. The 100- μm diameter is assigned as a reference diameter. The phase shift of the ripple structure of any diameter compared with the reference diameter is determined using the cross spectral density function [35] as detailed in Appendix C. Reference diameters at 80 and 120 μm are also simulated in order to see the effect of the absolute diameter. The phase shift versus diameter difference is shown in Fig. 4.3. It can be seen that, at diameter ranges from 80-120 μm the relations of phase difference and diameter difference are similar.

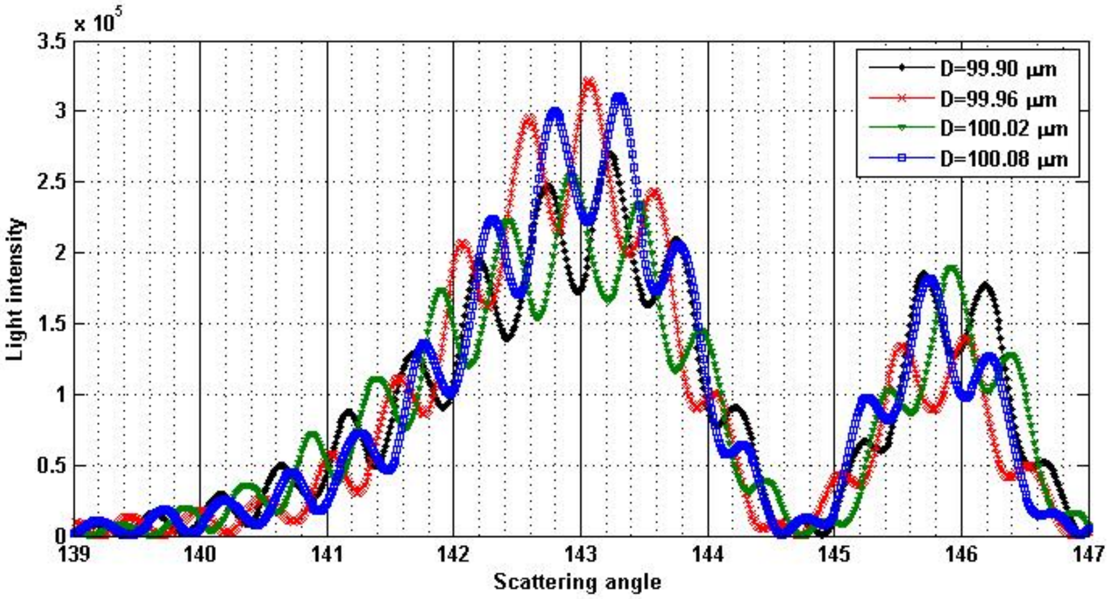

Figure 4.2: The simulated rainbow pattern based on the Lorenz-Mie Theory for the refractive index N=1.3600 and with droplet diameter varied from 99.90 μm to 100.08 μm

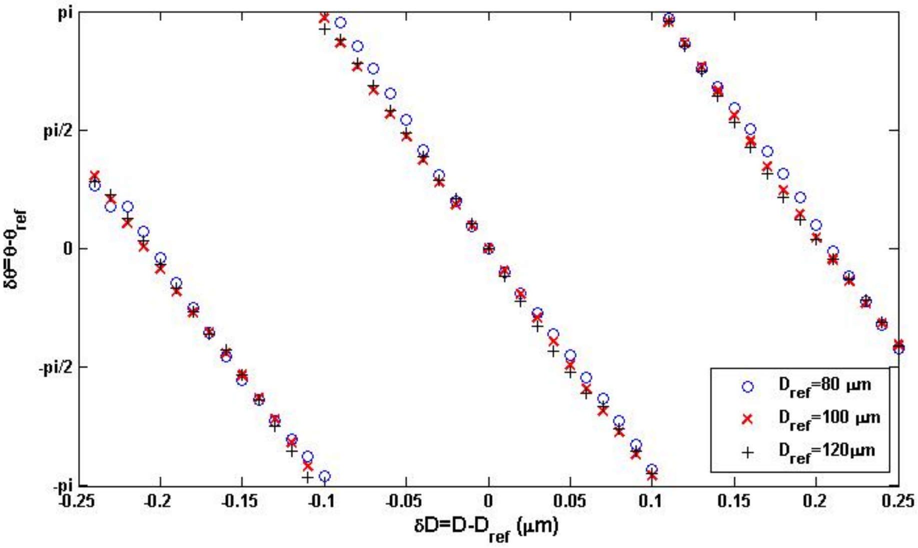

Figure 4.3: Phase shift of ripple structure versus diameter difference for droplet size 80-120 μm and refractive index 1.3600

The linear regression of Fig. 4.3 gives the correlation of phase shift and diameter change. In the range of one period ($0 \le \delta\theta \le 2\pi$), the relation can be written as:

$$\delta\theta = -30\delta D; \qquad |\delta D| \le 0.098 \text{ μm}. \tag{4.1}$$

When evaporation is the main purpose, the reduction of the diameter is considered. The change of diameter as a function of phase shift for the drop diameter 100±20 μm can be written as:

$$\delta D = \begin{cases} -\dfrac{1}{30}\delta\theta & ;\theta \ge 0 \\ -\dfrac{1}{30}\delta\theta - \dfrac{\pi}{30} & ;\theta < 0 \end{cases} \tag{4.2}$$

The relation can be used only for the case where the diameter decreases are smaller than 0.2 μm. The effects of refractive index have also been studied. It is found that this equation can be used for the refractive index range from 1.3500 to 1.3700 at the same range of diameter.

4.2 Experimental Setup

4.2.1 Mono-Disperse Drop Generator System

The MTG-01-G2 droplet generator made by FMP TECHNOLOGY GmbH type is used in this research. It uses the high frequency sound wave to break the liquid jet into a line of droplets. It has been developed for the generation of droplets with a constant and predictable size. The generated droplets can be from 40 μm up to 1000 μm in diameter, depending on the size of the pinhole and the operating parameters. The fluid is contained in a liquid feeder, the volume flow rate of which can be precisely adjusted. A filter is installed to trap contaminated particles to prevent clogging at the pinhole. The signal generator is connected to the piezo-ceramic vibrating element to break up the liquid jet into the line of droplets. In order to obtain stable and spherical droplets, operating parameters, such as the flow rate and the excitation frequency, have to be adjusted to appropriate conditions. The calculation of the operating parameters has been provided by the manufacturer and is reviewed in Appendix D. For this experiment, a 50 μm pinhole is used. The volume flow rate and the excitation frequency are 0.6 ml/min and 12-15 kHz, respectively. Corresponding to those parameters, the diameter of droplet is about 100-120 μm.

4.2.2 ORT Setup

The laser beam is transformed into a laser sheet by using a cylindrical lens. The horizontal slit is placed at the front of the 1st lens that allows us to collect the light scattered from droplet at the specified range of the vertical level. The experiments were carried out at the laboratory of CORIA-CNRS, France. The setup is shown in Fig 4.4. The diameter and focal length of the lenses used in this experiment are 75 mm and 150 mm, respectively. The distance between the measurement plane and the 1st lens and between 1st lens and 2nd lens are about 290 mm and 380 mm, respectively. The center of the measurement volume is at 50 mm away from the nozzle. The width of the front slit is 2 mm. The camera used in this experiment is 2048×2048 pixel^2 CCD camera. The exposure time is 60 ms and sampling rate is 15 frame/s.

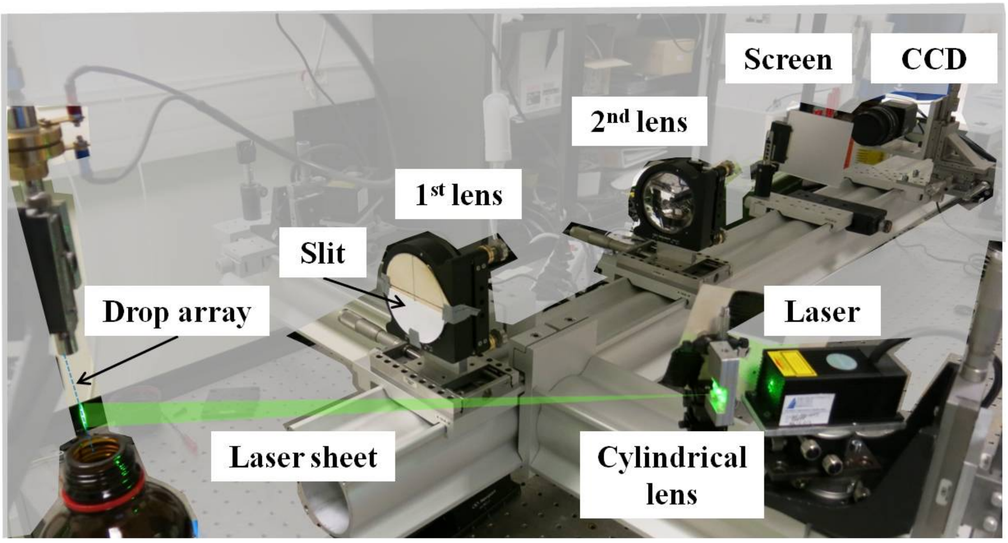

Figure 4.4: Experimental setup of ORT

4.2.3 Calibration

The vertical position of the rainbow signal appeared on the CCD camera corresponding to the vertical position of the droplet in the line measurement volume that was determined prior to the experiment. The schematic diagram of the calibration setup is shown in Fig 4.5. In the calibration, a piece of paper is put close to the line of droplet to obstruct the scattered light. The nozzle of the drop generator is installed on a micro-translator for vertical adjustment. When the nozzle is moved vertically at distance y, the edge of the paper appears on the screen with position y*'*. The corresponding pixel position in the recorded image is localized. The integrated rows corresponding to the distance y are presented in Table 4.1.

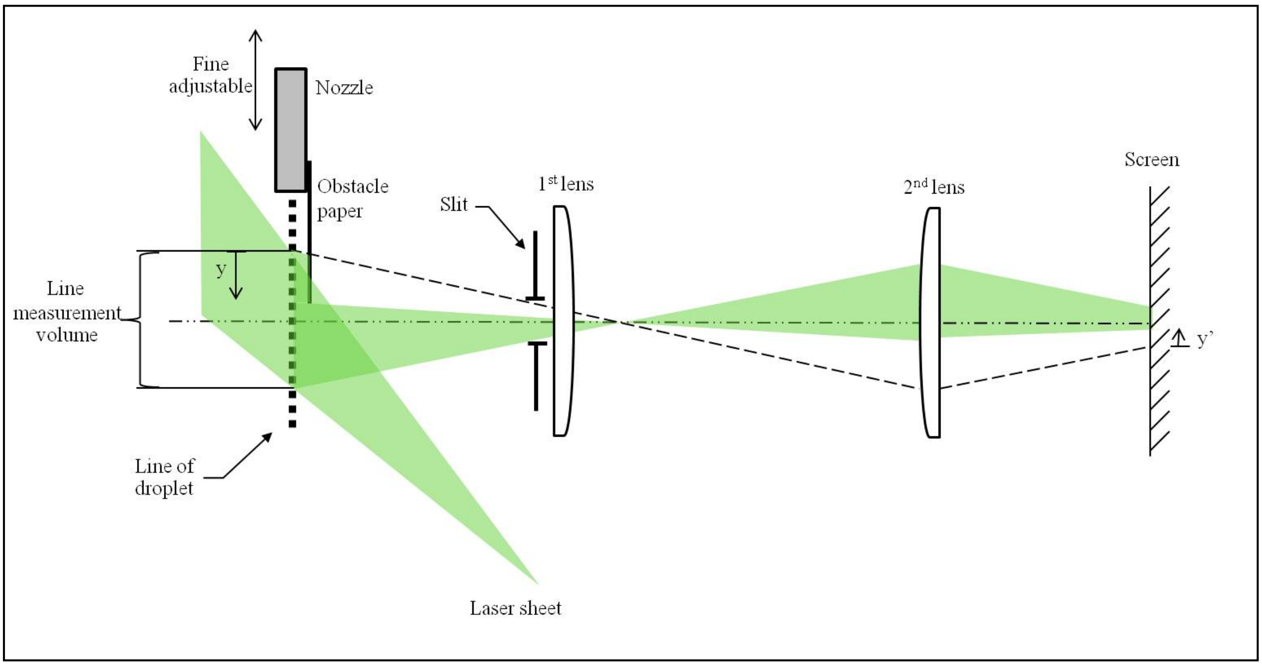

Figure 4.5: The calibration for the vertical distance of droplet

Table 4.1: The integrated rows corresponding to the vertical distance y of droplet

y (mm)	range of pixel
0	680-700
1	720-740
2	760-780
3	800-820
4	840-860
5	880-900
6	920-940
7	960-980
8	1000-1020

4.2.4 Data Extraction

A Matlab code is written to read the recorded rainbow image and calculate the phase shift and the diameter change. In the program, the image is read as a matrix size 2048×2048. From the calibration data in Table 4.1, the matrix is divided into 9 matrixes of size 21×2048. In each matrix, the intensity is averaged along the column; then 9 vectors of intensity distribution are obtained. The first vector at the top is assigned as the reference signal. Then, phase differences of the obtained 9 signals compared with the reference signal are calculated. Using the relation in Eq. 4.2, the diameter differences are determined. To test the calculation code, simulated rainbow image is used as the input data. The rainbow simulation program based on Lorenz-Mie theory is used in which the rainbow orders p=1 to p=10 are taken into account. We locate the simulated rainbow at row 680th to row 1020th of the camera size 2048×2048 pixel^2. The drop diameter is reduced by 0.2 nm within one row. The refractive index is 1.3600 and the initial drop diameter is 100 μm. The simulated rainbow image is shown in Fig. 4.6. The diameter differences calculated from the simulated rainbow image compared with the simulated diameters are shown in Fig. 4.7 with the rainbow signal at row 690th being the reference signal.

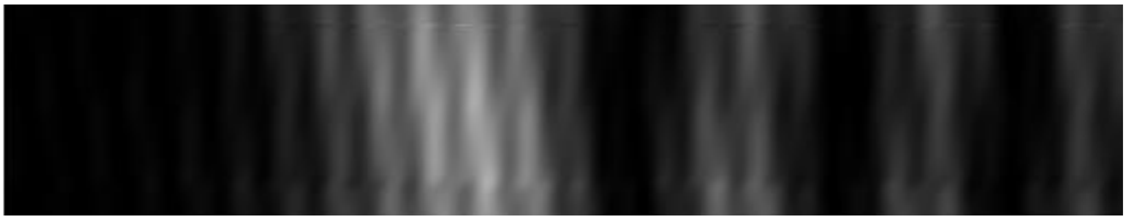

Figure 4.6: The simulated rainbow image of the droplet with refractive index 1.3600 and diameter decreases 0.2 nm in one row of pixels

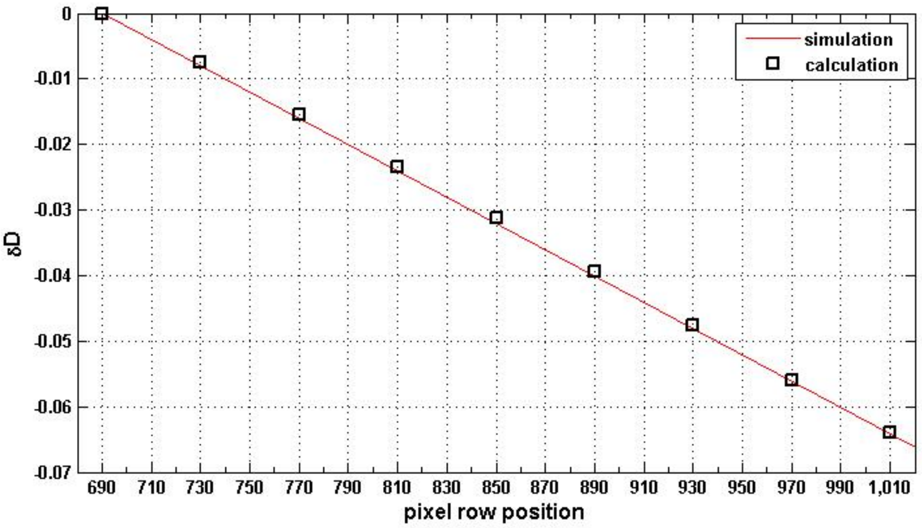

Figure 4.7: Drop diameter difference computed from the image in Fig. 4.6 compared to the simulated conditions

4.3 Results and Discussion

The line of ethanol droplets is left to evaporate under the room temperature at 20°C. The 5 series of experiments is repeated under the same conditions. In each series, 100 images are recorded continuously in 6.7 seconds. The typical rainbow image is shown in Fig. 4.8. The angle of ripple structure due to evaporation can be observed. From the top to bottom, the ripple structure moves from left (lower scattering angle) to the right (higher scattering angle) due to the decreasing of droplet diameter. The intensity distribution at the difference level is plotted in Fig. 4.9.

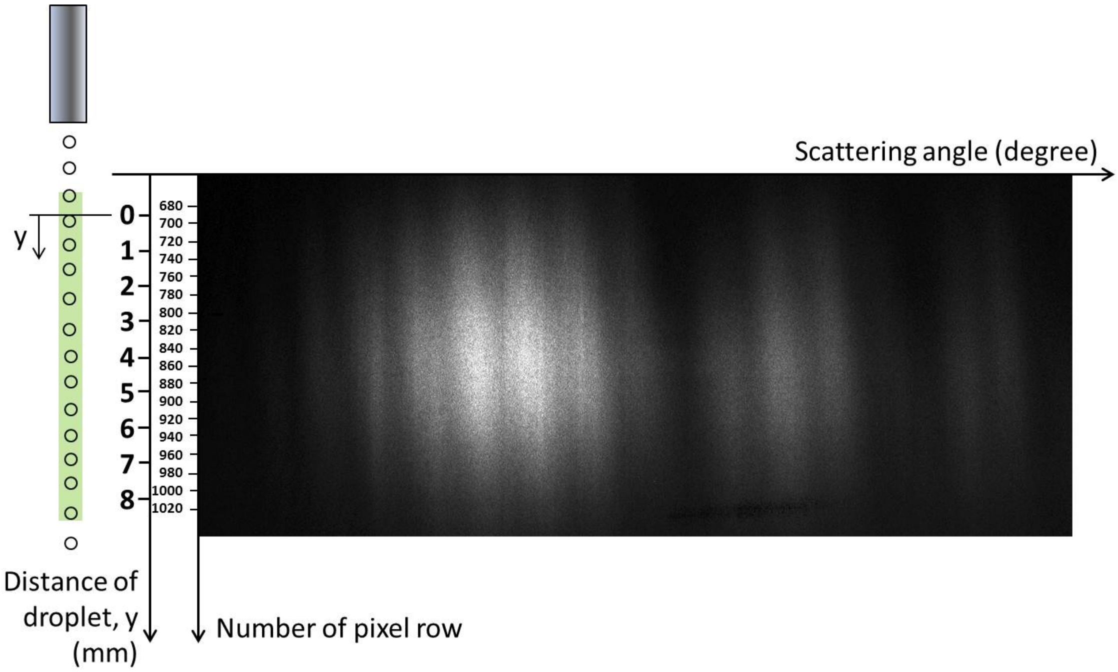

Figure 4.8: The recorded rainbow image and the selection of the integrated row

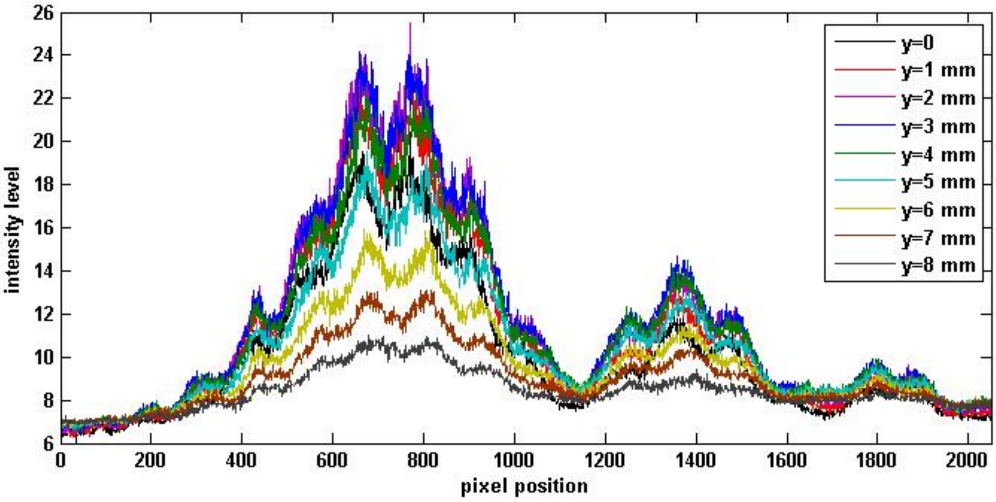

Figure 4.9: The intensity distribution of the rainbow signal at each level

4.3.1 Diameter Difference

The averaged diameter difference obtained from the 500 images is plotted with the standard deviation in Fig. 4.10. The deviation of the diameter mainly comes from the oscillation of the mono-disperse droplets. As can be seen, the drop diameter decreases only

65 nm in 8 mm length. The results show the ability of ORT to measure a very small change of diameter with the maximum standard deviation at 7.7%.

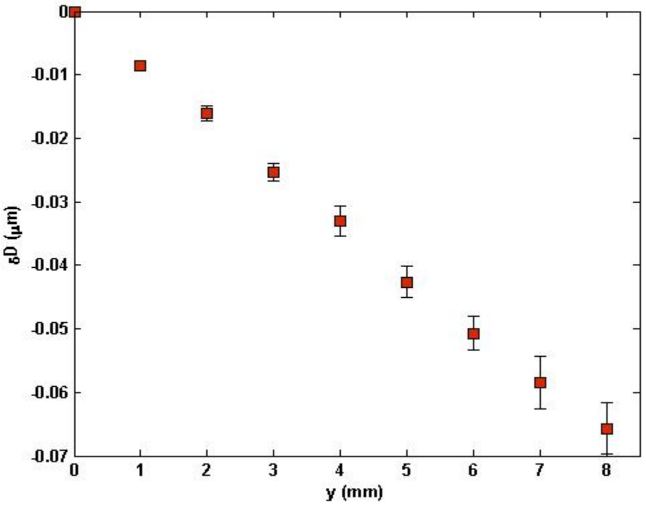

Figure 4.10: The averaged diameter difference obtained from 500 images with the standard deviation

4.3.2 Evaporation Constant

We apply the D^2-law of evaporation to estimate the evaporation constant from the known drop diameter difference as

$$(D_0 - \delta D)^2 = D_0^2 - \beta t), \tag{4.3}$$

The absolute diameter, D_0, is estimated from the following equation:

$$D_0 = \left(\frac{3ud^2}{2f} \right), \tag{4.4}$$

where d and f is the pinhole diameter and the excitation frequency, respectively. The jet velocity, u, can be calculated by:

$$u = \frac{4\dot{V}}{\pi d^2}, \tag{4.5}$$

when $\dot{V}$ is the volume flow rate. The time of evaporation is estimated from the velocity of the droplet. It was assumed to be equal to the jet velocity, *u*. Then, the vertical level of droplet, y, can be converted to the time, *t*, as:

$$t = \frac{y}{u} \tag{4.6}$$

Then, the D^2-t plot can be performed. As shown in Fig. 4.11, the linear regression can be fitted very well with the D^2-t plot. For the 500 images of the rainbow signal, the evaporation constant of ethanol evaporated into the air at 20°C is 0.008483±0.000513 mm^2/s.

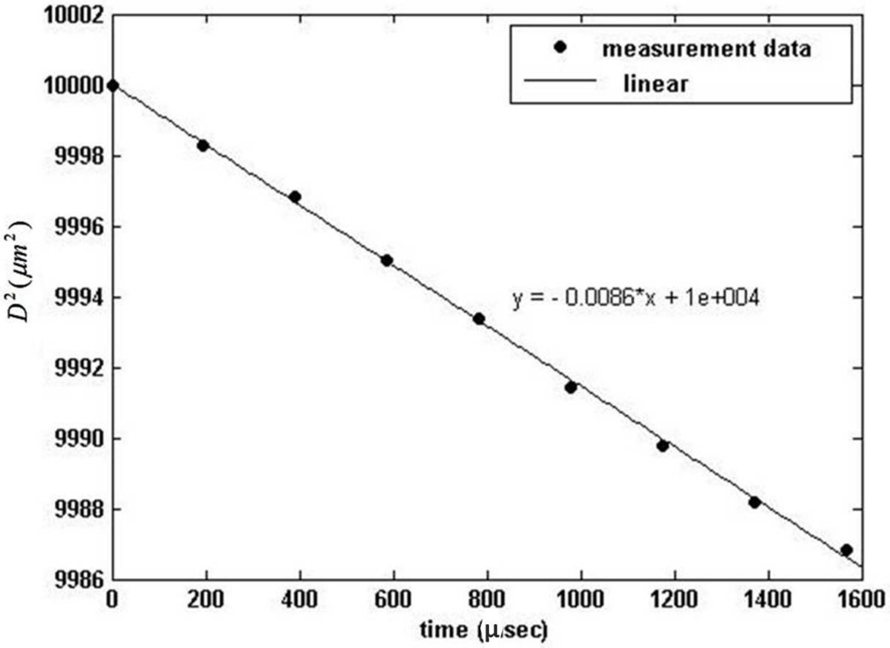

Figure 4.11: An example of D^2-t plot from the obtained diameter difference and the approximated D_0=100 µm and *u*=5.1 m/s

CHAPTER 5

CONCLUSIONS AND RECOMMENDATIONS

The development of an evaporation model based on the assumption of uniform and constant temperature (infinite conductivity of liquid) is the focus of this study. The states of fuel vapor at the interface such as surface temperature and partial pressure, can be estimated using the concept of the adiabatic saturation process. The exact solutions to the one-dimensional heat and mass transfer equations coupling with the mass continuity equation give the classical law of evaporation, namely D^2 law. These solutions can be used to calculate the evaporation constant of a droplet of pure substance. A numerical method has also been applied in the mass and heat transfer equation to determine the temperature and concentration gradient of fuel vapor from drop surface to the vicinity. It was found that the states of fuel vapor at the drop surface are controlled only by the ambient pressure and temperature.

The history of drop diameter and refractive index of the suspended drop water and ethanol under room temperature was measured by using the imaging technique and the Rainbow Technique. In the case of water, the value of the evaporation constant and the temperature obtained from the measurement and numerical model are in the good agreement. The relative humidity of the surrounding air has a significant effect on the evaporation of water drop. In case of ethanol, the effect of the suspender and laser power cannot be ignored. The presence of the fiber suspender and laser light increases the evaporation rate of ethanol droplet. The evaporation model is shown to underestimate the evaporation constant. The temperature of droplet is always the adiabatic saturation temperature of liquid that depends only on the ambient conditions. The transition in temperature occurs when the initial drop diameter is not the adiabatic saturation temperature.

The One-dimension Rainbow Technique (ORT) has the potential to measure the change in size of droplets in the line by observing the ripple structure. The rainbow angles do not significantly change during evaporation implying that the temperature of droplet is constant. With the approximated absolute drop diameter and the calculated droplet velocity, the plot of diameter squared versus time has been performed. The plot shows good linear regression and conforms to the D^2-law of evaporation. The slopes of regression lines represent the evaporation constants. The future work and the limitations of the techniques are described in Sections 5.1 and 5.2.

5.1 Future work

The One-dimensional Rainbow Technique has been successfully used to measure the evaporation rate of fuel spray in the form of monodisperse droplets. To realize the fuel combustion, the evaporation of liquid fuel under high temperature or in an combustion flame should be investigated.

5.2 Limitations

ORT is a technique that can be used to measure the change of size and refractive index of a line of droplets. For pure substance liquid, the obtained refractive index can be used to calculate the temperature of droplet if the relation between refractive index and temperature is available. In case of multicomponent liquid, the refractive index is a function of two parameters, temperature and composition, leading to the complexity in data extraction. Knowing the initial composition and temperature and evaporated mass calculated from the diameter change of droplet may allow us to estimate the temperature and composition of droplet during evaporation using the numerical method. However, the lacking of the relation between the refractive index and temperature and composition limits this technique to some liquid. In this work, the imaginary part of the refractive index is omitted because the liquid is highly transparent. Since the intensity of the detected signal is low when the imaginary part of liquid is high, the rainbow technique is limited with the liquid that consists of high imaginary part of refractive index.

LIST OF REFERENCES

[1] Warnatz, J., U. Maas, and R.W. Dibble, *Combustion*. Second Edition ed. 1999, New York: Springer-Verlag Berlin Heidelberg.

[2] Morin, C., C. Chauveau, and I. Gökalp, *Droplet vaporisation characteristics of vegetable oil derived biofuels at high temperatures.* Experimental Thermal and Fluid Science, 2000. **21**(1–3): p. 41-50.

[3] Hallett, W.L.H. and S. Beauchamp-Kiss, *Evaporation of single droplets of ethanol–fuel oil mixtures.* Fuel, 2010. **89**(9): p. 2496-2504.

[4] Abarham, M. and I.S. Wichman, *Mono-component fuel droplet evaporation in the presence of background fuel vapor.* International Journal of Heat and Mass Transfer, 2011. **54**(17–18): p. 4090-4098.

[5] Chauveau, C., M. Birouk, and I. Gökalp, *An analysis of the d2-law departure during droplet evaporation in microgravity.* International Journal of Multiphase Flow, 2011. **37**(3): p. 252-259.

[6] Spalding, D.B., *The combustion of liquid fuels.* Symposium (International) on Combustion, 1953. **4**(1): p. 847-864.

[7] Marshall, W.R., *Evaporation from drops Part I.* Chemical Engineering Progress, 1952. **48**(3): p. 141-146.

[8] Marshall, W.R., *Evaporation from drops Part II.* Chemical Engineering Progress, 1952. **48**(4): p. 173-180.

[9] Lefebvre, A.H., *Atomization and Spray*. 1989, Washington DC: Hemisphere Publishing Corp.

[10] Kuo, K., *Principle of Combustion*. 1986, Singapore: John Wiley&Sons.

[11] Moyle, A.M., P.M. Smidansky, and D. Lamb, *Laboratory Studies of Water Droplet Evaporation Kinetics*, in *12th Conference on Cloud Physics*. 2006: Madison, WI

[12] Lamb, D., A.M. Moyle, and W.H. Brune, *The Environmental control of individual aqueous particles in a cubic electrodynamic levitation system.* Aerosol Sci. Technol., 1996. **24**: p. 263-278.

[13] Gogos, G. and D.N. Pope, *Combustion of Moving Droplets and of Droplets Suspended within a Convective Environment: Transient Numerical Results*, in *7th International Workshop on Microgravity Combustion and Chemically Reacting Systems,*. 2003: Cleveland, Ohio. p. 161-164.

[14] Tantivoranukul, K. and P. Vallikul., *Application of D2-law to Determine Time Evolution Drop-size Distribution and Their Burn-out time*, in *World Renewable Energy Congress*. 2009: Bangkok, Thailand.

[15] Saengkeaw, S., *Refractive index measurements by Global rainbow refractometry for spherical and non spherical droplets*, in *International Symposium on Applications of Laser Technique to Fluid Mechanics*. 2008: Lisbon, Portugal.

[16] Saengkeaw, S., *Development of Novel Global Rainbow Technique for Characterizing Spray Generated by Ultrasonic Nozzle*, in *Chemical Engineering*. 2005, Chulalongkorn University: Bangkok, Thailand. p. 238.

[17] Sirignano, W.A., *Fluid dynamics and transport of droplets and sprays*. Second Edition ed. 2010, United States of America: Cambridge University Press.

[18] Cengel, Y.A. and M.A. Boles, *Thermodynamics and Engineering Approach*. Fifth Edition ed. 2006, Singapore: McGRAW-HILL.

[19] Stoecker, W.F. and J.W. Jones, *Refrigeration & Air Conditioning*. Second Edition ed. 1982, Singapore: McGraw-HILL.

[20] Laza, T., *Pilot test and theoretical analysis of evaporation of one and more component fuels.* Periodica Polytechnica, 2008. **52**(2): p. 67-70.

[21] Seers, P., W. Thomas, and S. Bruyere-Bergeron, *Determination of fuel droplet evaporation based on multiple thermocouple sizes*, in *49th AIAA Aerospace Sciences Meeting including the New Horizons Forum and Aerospace Exposition*. 2011: Orlando, Florida. p. 1-6.

[22] Maqua, C., G. Castanet, and F. Lemoine, *Bicomponent droplets evaporation: Temperature measurements and modelling.* Fuel, 2008. **87**(13–14): p. 2932-2942.

[23] Sazhin, S.S., *Advanced models of fuel droplet heating and evaporation.* Progress in Energy and Combustion Science, 2006. **32**(2): p. 162-214.

[24] Barata, J., *Modelling of biofuel droplets dispersion and evaporation.* Renewable Energy, 2008. **33**(4): p. 769-779.

[25] Nussenzveig, H.M., *High-Frequency Scattering by a Transperent Sphere I. Direct Reflection and Transmission.* Mathematical Physics, 1969. **10**(1): p. 82-124.

[26] Schiebener, P., et al., *Refractive index of water and steam an function of wavelength, temperature and density.* Journal of Physical and Chemical Reference Data, 1990. **19**(3): p. 677-717.

[27] Fujita, A., R. Kurose, and S. Komori, *Experimental study on effect of relative humidity on heat transfer of an evaporating water droplet in air flow.* International Journal of Multiphase Flow, 2010. **36**(3): p. 244-247.

[28] Yu, H., F. Xu, and C. Tropea, *Spheroidal droplet measurements based on generalized rainbow patterns.* Journal of Quantitative Spectroscopy and Radiative Transfer, 2013. **126**(0): p. 105-112.

[29] Castanet, G., M. Lebouché, and F. Lemoine, *Heat and mass transfer of combusting monodisperse droplets in a linear stream.* International Journal of Heat and Mass Transfer, 2005. **48**(16): p. 3261-3275.

[30] Maqua, C., et al., *Monodisperse droplet heating and evaporation: Experimental study and modelling.* International Journal of Heat and Mass Transfer, 2008. **51**(15–16): p. 3932-3945.

[31] Kristyadi, T., et al., *Monodisperse monocomponent fuel droplet heating and evaporation.* Fuel, 2010. **89**(12): p. 3995-4001.

[32] Frackowiak, B., et al., *Numerical analysis of the interactions between evaporating droplets in a monodisperse stream.* International Journal of Heat and Mass Transfer, 2010. **53**(7–8): p. 1392-1401.

[33] Saengkaew, S., et al., *Processing of individual rainbow signals.* Experiments in Fluids, 2010. **48**: p. 111-119.

[34] Wu, X., G. Grehan, and S. Saengkaew, *One-dimensional rainbow thermometry system by using slit apertures.* Optics Letters, 2014. **39**(3): p. 638-641.

[35] Domnick, J., H. Ertel, and T. Cameron, *Processing of Phase-Doppler Signal Using the Cross-Spectral Density Function.* Applications of Laser Anemometry to Fluid Mechanic, 1988. **4**: p. 473-483.

APPENDIXES

Appendix A: Airy Approximation

The Airy Theory is a scalar theory that describes the scattering of rays experimenting k internal reflections before leaving the spherical particle, but in a angular region close to the geometrical rainbow of order p. The Airy Theory is known to have a very limited range of application ($\alpha > 5000$, $\theta\text{-}\theta_R < 0.5^{\circ}$). The scattered intensity is given by:

$$I(\theta,\alpha) = (\varepsilon_1)^2 \left[\frac{81}{16\pi^2 h^2}\right]^{1/6} \cos\tau_p \ \alpha^{7/3} \ A_i^2(z) / \ \sin\theta_R, \tag{A1}$$

where A_i is the Airy function and z is:

$$z = (-q)\left[\frac{12}{h\pi^2}\right]^{1/3} \alpha^{2/3}\,(\theta - \theta_R), \tag{A2}$$

q is an integer equal to +1 or -1 in such a way that the rainbow angle is defined between 0 and π, and verify $2\pi l + q\theta_R = (\tau_p - p\tau'_p)$ with l an integer. τ_p and τ'_p are the complements of incident and refraction angles of the incident rainbow ray for p-1 internal reflection. N is the refractive index.

$$\tan\tau_p = \left[\frac{N^2-1}{p^2-N^2}\right]^{1/2}, \tag{A3}$$

$$\tan\tau'_p = \left[\frac{p^2(N^2-1)}{p^2-N^2}\right]^{1/2}, \tag{A4}$$

h is given by:

$$h = \left[\frac{(p^2-1)^2}{p^2(N^2-1)}\right]\left[\frac{p^2-N^2}{N^2-1}\right]^{1/2}, \tag{A5}$$

ε_1 is given by:

$$\varepsilon_1 = (1 - r_1^2)(r_1)^{(p-1)}, \tag{A6}$$

with:

$$r_1 = \frac{\sin(\tau_p - \tau'_p)}{\sin(\tau_p + \tau'_p)}, \tag{A7}$$

and the rainbow angle, θ_R, is calculated according to the theory of Descartes as:

$$\theta_R = 2\left\{p \cos^{-1}\left(\frac{1}{N}\sqrt{1 - \frac{N^2-1}{p^2-1}} - \sin^{-1}\sqrt{\frac{N^2-1}{p^2-1}}\right)\right\}. \tag{A8}$$

For the first and second rainbow, the order number, p, is 2 and 3, respectively.

Appendix B: Refractive Index of Water as a Function of Temperature [26]

The formulation of the wavelength, temperature and density dependence of the Lorenz-Lorenz function of light water and steam is:

$$\frac{n^2-1}{n^2+2}\frac{1}{\rho^*} = a_0 + a_1\rho^* + a_2T^* + a_3\lambda^{*2}T^* + a_4/\lambda^{*2} + \frac{a_5}{\lambda^{*2} - \lambda_{UV}^{*2}} + \frac{a_6}{\lambda^{*2} - \lambda_{IR}^{*2}} + a_7\rho^{*2} \tag{A9}$$

where

$\rho^* = \rho/\rho_0$ $\rho_0 = 1000$ kg/m3

$\lambda^* = \lambda/\lambda_0$ $\lambda_0 = 589$ nm

$T^* = T/T_0$ $T_0 = 273.15\text{K}$

and

$a_0 = +0.243905091$ $a_5 = +2.45733798\times10^{-3}$

$a_1 = +9.53518094\times10^{-3}$ $a_6 = +0.897478251$

$a_2 = -3.64358110\times10^{-3}$ $a_7 = -1.63066183\times10^{-2}$

$a_3 = +2.65666426\times10^{-4}$ $\lambda_{UV}^* = 0.2292020$

$a_4 = +1.59189325\times10^{-3}$ $\lambda_{IR}^* = 5.432937$

Note that the ranges of the three independent variables that have been used in the fit for such coefficients are:

Temperature: $0 < T < 225^o C$

Density: $0 < \rho < 1060\,\text{kg/m}^3$

Wavelength: $0.2 < \lambda < 2.5\mu\text{m}$

The refractive index of water at the wavelength 532 nm and temperature 0-30°C is plotted in Fig. A1.

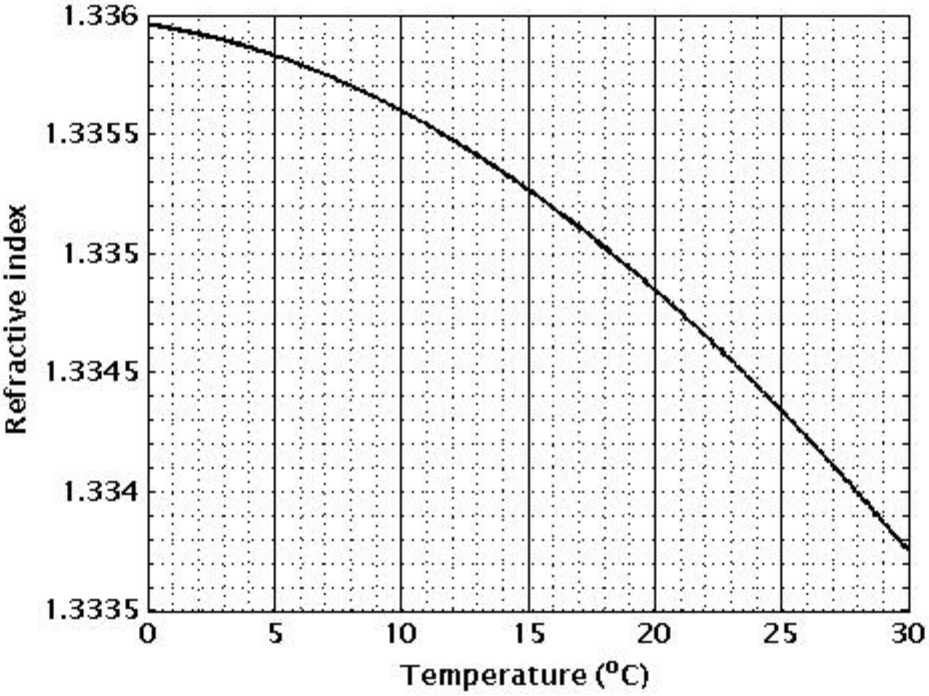

Figure A1: The refractive index of water at the wavelength 532 nm calculated from the relation formulated by Schiebener

Appendix C: Cross-Spectral Density Function for Phase Shift Determination [35]

The phase difference can be computed directly from the two signals by using a Fast-Fourier transformation such as:

$$G_{xy}(f_k) = \frac{2\Delta t}{N}|X_k^* Y_k| \, ; k = 0, 1, 2, \ldots, N-1 \tag{A10}$$

$$f_k = \frac{k}{N\Delta t} \tag{A11}$$

where X_k and Y_k are the discrete Fourier transformation (DFT) of the signals x(nΔt) and y(nΔt) respectively. The cross-spectral density function (CSD) is the series of the complex number consisting of the coincidence spectrum (real part) and quadrature spectrum (imaginary part), which can be written as:

$$G_{xy}(f) = C_{xy}(f) + jQ_{xy}(f) \tag{A12}$$

The magnitude and phase angle of that function can be determined by:

$$|G_{xy}(f)| = \sqrt{C_{xy}^2(f) + Q_{xy}^2(f)} \tag{A13}$$

$$\theta_{xy}(f) = tan^{-1}\left[\frac{Q_{xy}(f)}{C_{xy}(f)}\right] \tag{A14}$$

The Doppler frequency is identified by the peak of the magnitude of G_{xy}. Accordingly, the phase difference can be calculated via Equation (5). The resolution of the frequency measurement is limited by the sampling time, Δt, and the length or number of signal, N, as:

$$R = \frac{1}{N\Delta t} \tag{A15}$$

Therefore, to improve the accuracy of the obtained frequency, the points around the peak of $|G_{xy}(f)|$ are fitted to the parabolic function. Then, the vertex of the parabola is analytically determined as the Doppler frequency.

Appendix D: The Operating Parameter for Monodisperse Droplet Generator

(1) Theoretical Basics for Calculation of Process Parameter

The parameters that control the droplet formation are the size of pinhole, the excitation frequency and the liquid velocity or the flow rate. The stability criteria can be reached when the wavelength of deformation on jet surface is bigger than the circumference of the jet;

$$\frac{u_D}{f_G} \geq \pi D \tag{A16}$$

where u_D is the jet velocity, f_G is the excitation frequency and D is the pinhole diameter. The used scattering wave, which influences the fluid jet, produces droplets of the same size and predictable diameter D, if the dimensionless wavelength k is located at $0.3 \leq k \leq 0.9$, where

$$k = \frac{\pi D f_G}{u_D} \tag{A17}$$

From the equation above, the range of the excitation frequency, which can be used to create the monodisperse droplet, can be solved as:

$$\frac{0.3u_D}{\pi D} \leq f_G \leq \frac{0.9u_D}{\pi D} \tag{A18}$$

Then, the diameter of droplet, d, can be calculated from the following equation;

$$d = \left(\frac{3u_D D^2}{2f_G}\right)^{1/3} \tag{A19}$$

(2) Parameter selection

In case that the droplet diameter is desired, the selection can be done by the following step;

- The pinhole diameter

The pinhole diameter becomes the first parameter that should be selected properly, because it limits the droplet diameter. According to Equation A19, the droplet diameter, d, can be written in term of dimensionless wavelength, k, and pinhole diameter, D, as:

$$\mathrm{d} = \mathrm{D}\left(\frac{3\pi}{2\mathrm{k}}\right)^{1/3} \tag{A20}$$

Since k should be located at $0.3 \leq k \leq 0.9$, the range of the pinhole diameter becomes

$$0.40\mathrm{d} \leq \mathrm{D} \leq 0.57\mathrm{d} \tag{A21}$$

- The liquid flow rate

The flow rate for each size of pinhole provided by TSI Incorporated is used as a guide to approximate the liquid flow rate. As shown in Fig. A2, the 2nd order polynomial function is fitted with this data in order to determine the relation between the pinhole diameter and the flow rate. From the curve fitting, the obtained relation is:

$$\dot{\mathrm{V}} = 2.1974\times10^{-4} \cdot \mathrm{D}^2 - 5.8363\times10^{-4} \cdot \mathrm{D} + 0.0617 \tag{A22}$$

where $\dot{\mathrm{V}}$ is the volume flow rate in cm^3/min and D is diameter in μm.

- The excitation frequency

The range of the excitation frequency can be calculated from Equation A18, where the jet velocity is determined from the volume flow rate as:

$$u_D = \frac{\dot{V}}{A} \tag{A23}$$

where A is the cross section area, in this case is the area of the pinhole, that is

$$A = \frac{\pi D^2}{4} \tag{A24}$$

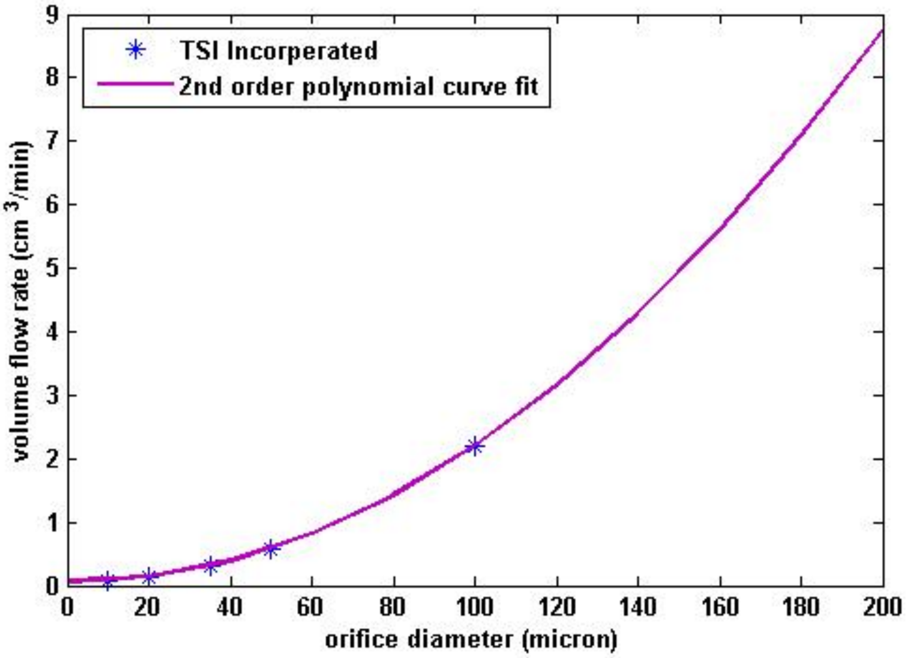

Figure A2: The volume flow rate for each orifice diameter provided by TSI Incorporated and its best curve fit